Quality Engineering

ISSN: 0898-2112 (Print) 1532-4222 (Online) Journal homepage: https://www.tandfonline.com/loi/lqen20

A statistics-guided approach to dimensional quality characterization of free-form surfaces with an application to 3D printing

Hao Wang, Qiong Zhang, Kaibo Wang & Xinwei Deng

To cite this article: Hao Wang, Qiong Zhang, Kaibo Wang & Xinwei Deng (2020) A statistics-guided approach to dimensional quality characterization of free-form surfaces with an application to 3D printing, Quality Engineering, 32:4, 721-739, DOI: 10.1080/08982112.2020.1740258

To link to this article: https://doi.org/10.1080/08982112.2020.1740258

QUALITY ENGINEERING
2020, VOL. 32, NO. 4, 721–739
https://doi.org/10.1080/08982112.2020.1740258

Taylor & Francis
Taylor & Francis Group

A statistics-guided approach to dimensional quality characterization of free-form surfaces with an application to 3D printing

Hao Wang[a], Qiong Zhang[b], Kaibo Wang[a], and Xinwei Deng[c]

[a]Department of Industrial Engineering, Tsinghua University, Beijing, China; [b]School of Mathematical and Statistical Sciences, Clemson University, Clemson, South Carolina; [c]Department of Statistics, Virginia Polytechnic Institute and State University, Blacksburg, Virginia

ABSTRACT

Free-from surfaces such as three-dimensional (3D) printing products play an important role in customized production of manufacturing. Despite its popularity, 3D printing products often suffer dimensional quality issues due to geometric deformation during the layer-by-layer printing process. Different from traditional production, 3D printing products are often customized and not for mass production, thus it is often difficult to designate tolerance profiles to assess the production quality. To address this challenge, we propose a statistics-guided approach to characterize the dimensional quality for free-form surfaces. The proposed approach can provide local quality measures based on the original customized design and the scanned profile of a printed product. It gives a unified scale of the quality assessment measurements to conveniently compare the quality of products from different customized designs. Case studies and simulation experiments show that, the proposed approach can provide effective quality assessment and characterization for 3D printing.

KEYWORDS

Dimensional quality; Gaussian process interpolation; multiple testing; quality assessment; smoothing

Introduction

By computer-aided-design (CAD), free-form surfaces play an important role in constructing 3D objects, which further offers a number of flexibilities to simplify the traditional manufacturing process. For example, 3D printing, led by free-form surfaces from CAD, produces customized surgical simulation models, prosthetics implants and surgery navigations (He et al. 2006; Rengier et al. 2010; Chen et al. 2015). However, 3D products often suffer from dimensional accuracy challenges (van Baar et al. 2018; Mohammed et al. 2016; Mazzoni et al. 2013; Cassetta et al. 2012), which are among the most important issues in the final parts. Mehra et al. (2011) summarize the accuracy characteristics of common types of 3D printers and point out that some of them can produce 1-2mm deviation. To meet the requirement of these high precision applications, it is desired to develop a quality assessment strategy to characterize the dimensional quality of free-form surfaces.

There are literature studies focusing on different aspects of dimensional accuracy evaluation of free-form surfaces. Li and Gu (2004) review general techniques to inspect free-form surfaces; Babu, Franciosa, and Ceglarek (2019) develop a spatio-temporal adaptive sampling method to effectively measure the free-form surface. Lasemi, Xue, and Gu (2010) analyze quality insurance of the CNC machining of free-form surfaces from the view of machining tool path and orientation. Another aspects about the dimensional deviation of free-form surfaces comes from geometric dimensioning and tolerancing (GD&T). Several papers (Krulikowski 1998; Ameta et al. 2015; Mahmood, Qureshi, and Talamona 2018) relate statistical measures with the design tolerances in 3D printing objects. However, it is often difficult to designate design tolerances for customized free-form surfaces such as 3D printing objects. Hence, the GD&T related techniques are not applicable in the quality control of free-form surfaces. Moreover, different from the traditional manufacturing, the deviation sources of 3D printing products are also from the dynamics of the thermo-mechanical processes of materials, which will cause layer adhesion, and geometric shrinkage and warping (Turner and Gold 2015; Ameta et al. 2015). Armillotta (2006) examines 3D printing surface quality from the layers and build orientations. However, existing studies are still far from sophisticated to assess dimensional quality of free-form surfaces.

CONTACT Qiong Zhang qiongz@clemson.edu School of Mathematical and Statistical Sciences, Clemson University, Clemson, SC, USA.

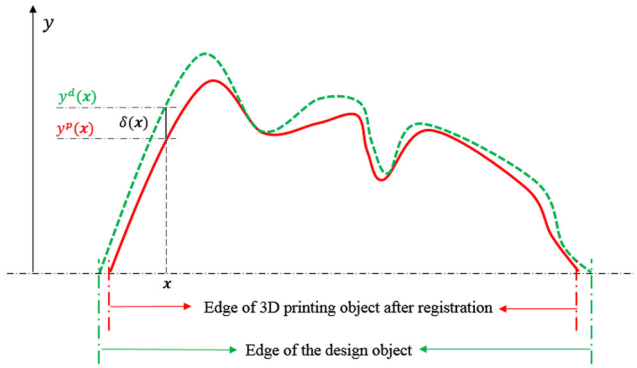

Figure 1. Illustration of dimension deviation of a 3D printing surface, y is the building direction and (x_1, x_2)–plane is the datum reference. $\delta(\boldsymbol{x})$ is the dimensional deviation on location $\boldsymbol{x}$.

In quality monitoring of free-form surfaces, Zang and Qiu (2018a,2018b) are among the most significant studies to provide quality control methods for 3D printing free-form surfaces. Note that their study is to analyze the whole surface quality in sequential and identical 3D printing process. Pechenin, Bolotov, and Rusanov (2014) adopt wavelets method to deal with profile-form and shaped free-form surfaces. Poniatowska (2009) analyzes the spatial autocorrelation of free-form surface deviations, and shows that there are significant spatial autocorrelation in the manufacturing of 3D free-form surfaces. However, the dimensional quality criterion in those studies are often defined as global criteria, whereas the quality heterogeneity in different areas has not been fully investigated. For quality assessment of free-form surfaces, it is critical to provide local quality measures, which often relies on the development of deformation models.

Sabbaghi et al. (2014) and Huang (2016) discuss the functional form of deformation models to characterize the cookie-like or cylinder-like outer-bound deformation and provide compensation based on polar coordinates. The unknown parameters in their deformation models can be determined based on the data collected from 3D scanning of the printed products. As an extension, Luan and Huang (2015) propose polygon and circular approximations for two-dimensional free-form products. The profiles of 2D design can be designated by explicit functions, whereas it cannot be applied to most of the irregular 3D computer-generated designs. Therefore, it is challenging to develop an appropriate and flexible model to characterize the dimensional quality by extending 2D profiles to 3D objects.

The main contribution of this work is to develop a framework for the dimensional quality characterization on local areas of free-form surfaces, which can be applied to many real production scenarios, include 3D printing process. We propose to model the deformation of free-form surfaces by Gaussian process. Based on collected 3D scanning data, the proposed model can provide deviation estimate over the entire surface. A self-adaptive L_2 penalized smoothing algorithm and a multiple testing approach are used to generate the quality characterizations and provide quality evaluation of local areas. The proposed framework provides standardized quality assessments for 3D printing surfaces. The merits of the proposed dimensional evaluation and assessment are elaborated through several 3D printing applications.

The remainder of the manuscript is organized as follows. Section "Gaussian process based deformation model" describes the Gaussian process based deformation model; Section "Quality assessment and characterization" proposes the dimensional quality characterization approach. Sections "Case study I" and "Case study II" provide case studies to validate the assumptions for geometric deformations and show the effectiveness of the proposed approach. Section "Simulation study" shows additional simulation experiments using synthetic data sets. We conclude this paper with a discussion in Section "Discussion."

Gaussian process based deformation model

This section introduces a Gaussian process approach to characterize the dimensional deviation of 3D printing. Previous studies in machining process only consider the dimensional errors from the probing direction (Desta, Feng, and Ouyang 2003; Xia, Ding, and Wang 2008). However, as pointed by Xiao et al. (2018), the geometric of 3D printing parts are significantly affected by the building direction, which implies that all the dimensional features have a common datum reference. Therefore, for parts with continuous surfaces, characterizing from the building direction is reasonable. We adopt the Cartesian coordinates system (x_1, x_2, y) to characterize the geometric shape of the 3D design, where y is the building direction and (x_1, x_2)–plane is the datum reference. Let $y_p(\boldsymbol{x})$ be the printed object based on the design surface $y_d(\boldsymbol{x})$. The design surface is denoted by $y_d(\boldsymbol{x})$, where $\boldsymbol{x} = (x_1, x_2) \in \mathcal{D}$, and $\mathcal{D}$ is the domain of the design surface. Without loss of generality, we assume that $\mathcal{D} = [0, 1]^2$. Thus, after registration, the deformation is characterized by dimensional deviation along the y-axis.

As shown in Figure 1, the dimensional deviation on location $\boldsymbol{x}$ can be defined by

$$\delta(\boldsymbol{x}) = y_d(\boldsymbol{x}) - y_p(\boldsymbol{x}), \quad \text{for any } \boldsymbol{x} \in \mathcal{D}. \tag{1}$$

A positive $\delta(\boldsymbol{x})$ indicates the surface shrinkage, whereas a negative $\delta(\boldsymbol{x})$ indicates the surface inflation. By 3D scanning of a printed product, we are able to obtain the measures of $y_p(\boldsymbol{x})$ over a discrete domain $\mathcal{P}_N \subset \mathcal{D}$ of size N. Thus the deformation value $\delta(\boldsymbol{x})$ can be calculated directly over $\mathcal{P}_N$.

To characterize the spacial dependence on the deformation surface and conduct statistic tests, we model $\delta(\boldsymbol{x})$ as a Gaussian process

$$\delta(\boldsymbol{x}) \sim \mathcal{GP}(0, \sigma^2 k(\boldsymbol{x}, \boldsymbol{x}'; \boldsymbol{\theta})), \tag{2}$$

where the global mean is assumed to be zero, $k(\boldsymbol{x}, \boldsymbol{x}'; \boldsymbol{\theta})$ is a correlation function, and σ^2 is the global variance. In this study, we adopt a separable exponential correlation function as

$$k(\boldsymbol{x}, \boldsymbol{x}'; \boldsymbol{\theta}) = \exp(-\theta_1|x_1 - x_1'| - \theta_2|x_2 - x_2'|), \tag{3}$$

where $\boldsymbol{\theta} = (\theta_1, \theta_2)$ is the correlation parameter. Computational detail of parameter estimation is deferred to Appendix A. The use of Gaussian process (GP) is a convenient way to model the spatial dependency on the deformation surface. Though the GP is a nonparametric method in nature, it provides a parametric framework to conduct hypothesis testing and make inference.

Choosing appropriate correlation function for GP has been discussed in literature (Diblasi and Bowman 2001; Maglione and Diblasi 2004; Paulo 2005). Bayarri et al. (2007) discuss the validation of using separable exponential correlation in computer experiments. In our application of the fused deposition modeling (FDM) 3D printing process, due to the nozzle moving along a specific direction, there could exist covariance heterogeneity along x_1 and x_2 axis. For other kinds of selective laser sintering (SLS) technique, it can also contain heterogeneity because the laser beam sweeps along a specific direction. Thus, it would be beneficial to consider the potential heterogeneity from both x_1 and x_2 directions in the printing process. Here we adopt the separable exponential correlation function to provide different measures of the strength of dependence along these two directions. The values of θ_1 and θ_2 can be viewed as a weighting scheme with respect to the horizontal and vertical axes.

Another reason of choosing the covariance function in (3) is to facilitate the computation for parameter estimation. As explained in Appendix A, the fast parameter estimation is very simple after computing a matrix M. In addition, the spatial structure in our application is dense in comparison with other applications. The collected samples are also quite intensive. Consequently, the results of the Gaussian process are not so sensitive to the selection of covariance function. We will validate this point in the case study in Section "Case study I."

It is worth noting that the test domain $\mathcal{P}_M$ can be easily established on a regular grid. The original scanned data of a 3D printing product are usually not in a regular grid since the angle of illumination will change in the scanning process. However, due to the high precision of the laser scanner, we will obtain a relatively dense point cloud after measurement. Thus, we can reconstruct a regular grid from the original irregular datasets. Since the density of the original data is sufficient, the extraction of grid data will not introduce significant error. In our application, the absolute distance between the exact extracted location and the ideal extracted location is controlled to be smaller than 0.04 mm, which is smaller than the precision of the laser scanner (0.05 mm).

Let $\Delta\boldsymbol{y}$ be a vector of size N collecting the deviation values $\delta(\boldsymbol{x})$ for all $\boldsymbol{x} \in \mathcal{P}_N$. Based on the Gaussian process model fitted by $\Delta\boldsymbol{y}$, we evaluate the deviation over a test domain $\mathcal{P}_M \subset \mathcal{D}$ of size M. Let $\mathcal{P}_M \triangleq \{\boldsymbol{x}_1^*, ..., \boldsymbol{x}_M^*\}$, and $\boldsymbol{\delta} = (\delta(\boldsymbol{x}_1^*), ..., \delta(\boldsymbol{x}_M^*))^\top$ be the deviation vector over the test domain $\mathcal{P}_M$. There can be different focuses on the test domain. In some scenarios, the focuses are on several specific locations, for example at some critical dimensions. In other scenarios, they may focus on uniformly distributed dimensional quality. The proposed quality evaluation framework provides this flexibility to establish test domain as needed. Note that extrapolation should be avoided. Thus, the test domain should be included in the measurement domain. Under the Gaussian process assumption in (2), the best linear unbiased predictor of $\delta(\boldsymbol{x}_i^*)$ can be expressed by

$$\hat{\delta}(\boldsymbol{x}_i^*) = \boldsymbol{r}(\boldsymbol{x}_i^*)^\top \boldsymbol{R}^{-1} \Delta\boldsymbol{y}, \tag{4}$$

where $\boldsymbol{r}(\boldsymbol{x}_i^*) = [k(\boldsymbol{x}_i^*, \boldsymbol{x}_1; \boldsymbol{\theta}), ..., k(\boldsymbol{x}_i^*, \boldsymbol{x}_N; \boldsymbol{\theta})]^\top$ with $\boldsymbol{x}_1, ..., \boldsymbol{x}_N$ be the points in $\mathcal{P}_N$, and $\boldsymbol{R}$ is an $N \times N$ the correlation matrix over the domain $\mathcal{P}_N$.

Based on the Gaussian process model, the estimated deviation $\hat{\boldsymbol{\delta}} = (\hat{\delta}(\boldsymbol{x}_1^*), ..., \hat{\delta}(\boldsymbol{x}_M^*))$ follows a multivariate normal distribution with a covariance matrix $\boldsymbol{\Sigma}_{\hat{\delta}}$. Also, each $\hat{\delta}(\boldsymbol{x}_j^*)$ has mean and variance as:

$$E(\hat{\boldsymbol{\delta}}(x_j^*)) = \boldsymbol{r}(\boldsymbol{x}_j^*)^\top \boldsymbol{R}^{-1} E(\Delta\boldsymbol{y}) = 0$$
$$\mathrm{Var}(\hat{\boldsymbol{\delta}}(x_j^*)) = \sigma^2 \boldsymbol{r}(\boldsymbol{x}_j^*)^\top (\boldsymbol{R}^{-1}) \boldsymbol{r}(\boldsymbol{x}_j^*)$$

It can be converted to a z-statistic following the standard normal distribution:

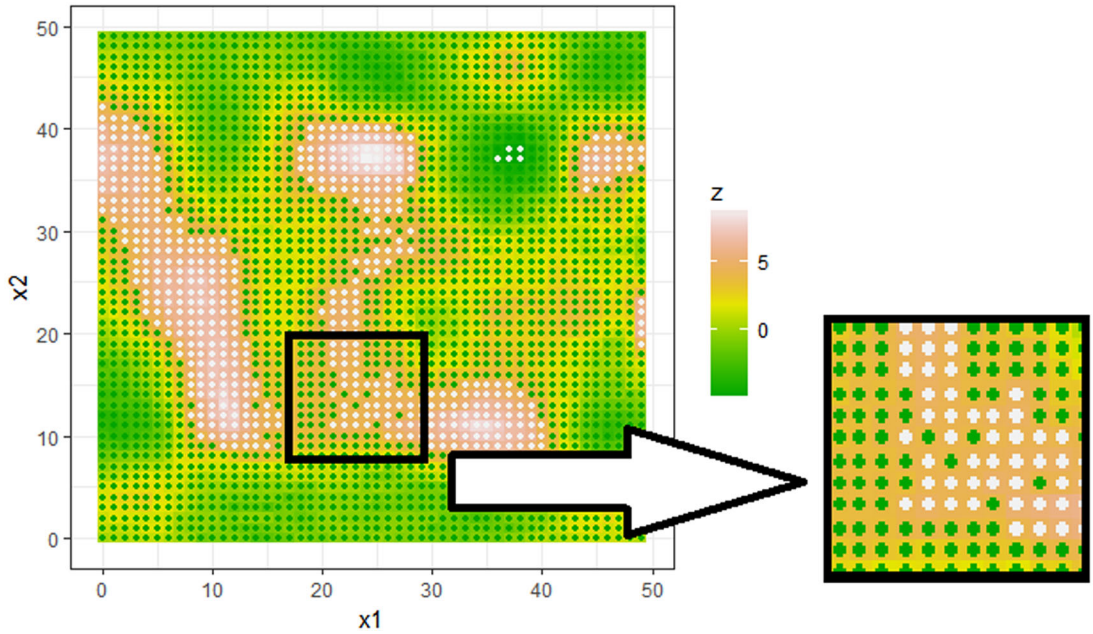

Figure 2. Significant test results based on z_j values. Discrete insignificant locations scattered in significant locations. The significant and un-significant results are also shown by light and dark spots on the test locations.

$$z_j \triangleq \frac{\hat{\delta}(\boldsymbol{x}_j^*) - \mathrm{E}(\hat{\delta}(\boldsymbol{x}_j^*))}{\sqrt{\mathrm{Var}(\hat{\delta}(\boldsymbol{x}_j^*))}} \sim \mathcal{N}(0,1). \tag{5}$$

We further develop the quality characterization based on the normality of the predicted deviation.

Quality assessment and characterization

Processing of original Z-statistics

The dimensional quality of the printed object can be different in local areas. We propose a multiple testing based approach to assess and characterize the local quality in this Section. Before conducting assessment, z_j should be processed in advance. The reasons are stated as follows. An absolute value of z_j larger than a threshold value indicates a significant geometric deformation on location j. However, when the test domain is too dense, or due to the insufficient precision in the measuring process, noises exist in the evaluation results. Due to the noise, the signals are not automatically separated into continuous local regions, there might be discrete signals appearing in some local areas, as demonstrated in Figure 2. To remove the noise, we develop a local smoothness algorithm to de-noise the signals before local quality assessment.

We scale the value of the original z-statistics in (5) by nonparametric smoothing. There are two reasons that we do not apply a parametric model to characterize the underlying deformation. First, compared with local smoothing method, a parametric model needs a stronger assumption for the functional form of deformation, which is not available for customized 3D printing. Second, local smoothing is more preferential in maintaining the local features of the deformation information. Further discussions can be found in Walker and Wright (2002).

We would remark that the cubic smoothing spline is a well-known method for curve fitting, of which the challenge is on the selection of knots and smoothing parameters. Our proposed method is designed for relatively sparse and regular gird. Based on the robust GCV algorithm designed on lattice in Section "An algorithm to determine the smooth parameter," the smoothing spline method appears being suitable to generate more reasonable smoothing results.

We propose an L_2 penalized smoothing approach to remove the inherent noise in the test statistics $\boldsymbol{z} = [z_1, ..., z_M]$. Under a pre-specified smoothing parameter s, the smoothed test statistics $\boldsymbol{z}^{(s)}$ is defined as the minimizer of the L_2 penalized residuals sum-of-square (RSS) of the original $\boldsymbol{z}$:

$$\boldsymbol{z}^{(s)} = \underset{\tilde{\boldsymbol{z}} \in \mathcal{R}^M}{\mathrm{argmin}} \left\{ \sum_{j=1}^{M} \{z_j - \tilde{z}_j\}^2 + s \sum_{j=1}^{M} \{d_2(\tilde{z}_j)\}^2 \right\} \tag{6}$$

where d_2 indicates the second-order difference at location j, and $\tilde{\boldsymbol{z}} = (\tilde{z}_1, ..., \tilde{z}_M)^\top$ is a vector collecting the linear parameters. The RSS term in (6) maintains the original quality information in $\boldsymbol{z}$, and the L_2 penalty

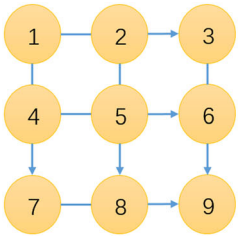

$$\boldsymbol{D} = \begin{bmatrix} 1 & -2 & 1 & & & & & & \\ & & & 1 & -2 & 1 & & & \\ & & & & & & 1 & -2 & 1 \\ 1 & & & -2 & & & 1 & & \\ & 1 & & & -2 & & & 1 & \\ & & 1 & & & -2 & & & 1 \end{bmatrix}$$

Figure 3. A 3×3 regular grid and corresponding matrix $\boldsymbol{D}$.

term controls the degree of smoothness. As s increases, the level of smoothness increases. According to Tepper and Sapiro (2012), the L_2 penalty is more sensitive to extreme values than the L_1 penalty. Therefore, the quality information about $\boldsymbol{z}$ will not be eliminated by over smoothing. Notice that, (6) is a special case of the smoothing spline estimation (see for example, Green and Silverman 1993).

Then the objective function in (6) can be rewritten as

$$\boldsymbol{z}^{(s)} = \underset{\tilde{\boldsymbol{z}} \in \mathcal{R}^M}{\operatorname{argmin}} \{(\boldsymbol{z} - \tilde{\boldsymbol{z}})^\top (\boldsymbol{z} - \tilde{\boldsymbol{z}}) + s\tilde{\boldsymbol{z}}^\top \boldsymbol{D}^\top \boldsymbol{D}\tilde{\boldsymbol{z}}\}. \tag{7}$$

where $\boldsymbol{D}$ is a matrix providing the information of second-order difference. For a test domain with M locations, $\boldsymbol{D}$ is a matrix with $2\sqrt{M}\left(\sqrt{M}-2\right)$ rows and M columns. Each row of $\boldsymbol{D}$ indicates a second-order difference along the two directions of the test domain. As illustrated with Figure 3, for the j-th row, $D_{ij} = -2$ indicating that j is the current site on which the difference is being calculated, whereas $D_{ij'} = 1$ indicating that j' is the site adjacent to the site i.

Given s, the smoothed statistic $\boldsymbol{z}^{(s)}$ in (7) can be efficiently obtained by the eigen-decomposition of $\boldsymbol{D}^\top \boldsymbol{D}$, i.e.,

$$\boldsymbol{z}^{(s)} = (I_M + s\boldsymbol{D}^\top \boldsymbol{D})^{-1}\boldsymbol{z} = \left(I_M + sU\operatorname{diag}(\lambda_1, \ldots, \lambda_M)U^\top\right)^{-1}\boldsymbol{z} = A(s)\boldsymbol{z} \tag{8}$$

where $A(s) = U\Lambda^{-1}(s)U^\top$, and $\Lambda(s)$ is a $M \times M$ diagonal matrix with i diagonal entry $1 + s\lambda_i$.

An algorithm to determine the smooth parameter

In this section, we develop an algorithm to determine the smooth parameter s. We adopt a RGCV (Robust Generalized Cross-validation) measure, originally proposed by (Lukas 2006), to choose the optimal smooth parameter s:

$$\begin{aligned} s^{opt}(\gamma) &= \arg\min_s \bar{V}(s;\gamma) \\ &= \arg\min_s \{\gamma V(s) + (1-\gamma)F(s)\}, \end{aligned} \tag{9}$$

where

$$V(s) = \frac{M||\{I - A(s)\}\boldsymbol{z}||^2}{\operatorname{tr}^2\{I - A(s)\}}, \quad F(s) = \operatorname{tr}\{A(s)^2\}V(s)/M,$$

and γ is the robust parameter. By including $F(s)$ into the selection criterion, RGCV penalizes the values of s that are close to 0. As γ gradually decreases from 1 to 0, the optimal $s^{opt}(\gamma)$ become more robust and less likely to be a small value. This combination can provide a tradeoff between maintaining original signals and the final smoothing effect. The choice of γ is greatly associated with the data. It can be determined by observation as described in Lukas (2006). In our study, the choice of γ can be greatly different on datasets collected from different 3D design models. To avoid manually searching the ideal values of these parameters, we develop an auto-selection procedure to choose the robust parameter γ and the smooth parameter s.

The proposed auto-selection procedure can be described in four steps: (1) designate sequences $\Gamma = [\gamma_1, \ldots, \gamma_k, \ldots, \gamma_K]$ and $\mathcal{S} = [s_1, \ldots, s_i, \ldots, s_I]$ as the search spaces of s and γ, respectively; (2) for each $\gamma_k \in \Gamma$, obtain $s^{opt}(\gamma_k) = \arg\min_{s\in\mathcal{S}} \bar{V}(s;\gamma)$; (3) calculate the shift $\Theta(k)$ at the current step by

$$\Theta(k) = \frac{2|s^{opt}(\gamma_{k+1}) + s^{opt}(\gamma_{k-1}) - 2s^{opt}(\gamma_k)|}{|\gamma_{k+1} - \gamma_{k-1}|};$$

(4) choose optimal $\gamma^* = \gamma_{k^*}$ when the shift $\Theta(k)$ becomes stable, i.e.,

$$k^* = \min\{k \in [2, \ldots, K-1] \ |\Theta(k) < \theta\}, \tag{10}$$

where θ is a pre-specified threshold value. To illustrate the selection procedure, Figure 4a shows the relationship between the shift of optimal s and γ, whereas 4(b) provides different RGCV paths, and indicates that our procedure can choose a proper robust parameter γ. Since changes in s^{opt} will be insignificant when γ is large enough, the result is not sensitive to the choice of the threshold θ. We fix θ to be 0.05 in our case studies and numerical experiments. The procedure to determine the smoothing parameter and the robust parameter is summarized in Algorithm 1.

Algorithm 1: Choose proper $\gamma^* \in \Gamma$

Input: data size M, original $\boldsymbol{z}^*$, edge indicate matrix $\boldsymbol{D}$, Eigen decomposition $\boldsymbol{D}^\top\boldsymbol{D} = \boldsymbol{U}diag\{\lambda_1, ..., \lambda_m, ..., \lambda_M\}\boldsymbol{U}'$, Searching sequence $\mathcal{S} = [s_1, ..., s_i, ..., s_I]$, Searching sequence $\Gamma = [\gamma_1, ..., \gamma_k, ..., \gamma_K]$

Output: Proper robust parameter $\gamma^* \in \Gamma$.

Init: $\boldsymbol{s}^{opt} \leftarrow \text{vec}(K), \boldsymbol{\Theta} \leftarrow \text{vec}(K)$, γ, k^*, γ^*

for $k \leftarrow 1$ ***to*** K **do**

$\gamma = \gamma_k$

$\boldsymbol{V} \leftarrow \text{vec}(I)$; $\boldsymbol{tr}_{A^2} \leftarrow \text{vec}(I)$; $\boldsymbol{uz} \leftarrow \boldsymbol{U}^\top\boldsymbol{z}^*$; s^{opt}; i^*

for $i \leftarrow 1$ ***to*** I **do**

$$\boldsymbol{V}(i) \leftarrow \frac{M^{-1}\sum_{m=1}^{M}\lambda_m(uz(m))^2}{(M^{-1}\sum_{m=1}^{M}s_i\lambda_m/(1+s_i\lambda_m))^2}$$

$$\boldsymbol{tr}_{A^2}(i) \leftarrow \sum_{m=1}^{M}1/(1+s_i\lambda_m)^2$$

$i^* \leftarrow \arg\min_i\{[\gamma + (1-\gamma)\boldsymbol{tr}_{A^2}(i)/M]\boldsymbol{V}(i)\}$

$s^{opt}(k) \leftarrow s_{i^*}$

for $k \leftarrow 2$ ***to*** $K-1$ **do**

$$\Theta_k \leftarrow \frac{|s^{opt}(k+1) - 2s^{opt}(k) + s^{opt}(k-1)|}{|\gamma_{k+1} - \gamma_{k-1}|/2}$$

$k^* = \min\{k \in [2, ..., K-1] |\ \Theta(k) < \theta\}$

$\gamma^* = \gamma_{k^*}$

return $\{\gamma^*\}$

Statistics guided quality assessment and characterization

As described in Section "Gaussian process based deformation model," we obtain the estimated deviation vector $\hat{\boldsymbol{\delta}} = (\hat{\delta}(\boldsymbol{x}_1^*), ..., \hat{\delta}(\boldsymbol{x}_M^*))$ in (4) over the test domain $\mathcal{P}_M$. Based on $\hat{\boldsymbol{\delta}}$, we propose a multiple hypothesis testing approach to assess the local quality of the printed object. For local area with good quality, the expected value of $\hat{\delta}(\boldsymbol{x})$ is zero. Therefore, for each location $j = 1, 2, ..., M$ in $\mathcal{P}_M$, we test the hypothesis:

$$H_{j0} : \text{E}(\hat{\boldsymbol{\delta}}(\boldsymbol{x}_j^*)) = 0 \text{ v.s. } H_{ja} : \text{E}(\hat{\boldsymbol{\delta}}(\boldsymbol{x}_j^*)) \neq 0. \quad (11)$$

According to the Gaussian assumption in (2), z_j in (5) is the test statistic of H_{j0}. A higher absolute value of z_j indicates lower local quality and severer geometric deformation.

For quality assessment purpose, the goal is to obtain p-values of H_{j0} in (11) for $j = 1, ..., M$. Define E_j as "reject H_{j0} when H_{j0} is true". The family-wise error rate (FWER) $\sum_{j=1}^{M}P(E_j|H_{0j})$ is used to provide the family-wise rejection criteria c_m. Notice that, the smoothed test statistics $\boldsymbol{z}^{(s)}$ can be expressed by

$$\boldsymbol{z}^{(s)} = A(s)\boldsymbol{z} = A(s)D_g^{-1/2}\hat{\boldsymbol{\delta}} \triangleq \boldsymbol{F}\hat{\boldsymbol{\delta}}, \quad (12)$$

where $D_g = \text{diag}\{\text{Var}(\hat{\boldsymbol{\delta}}(x_1^*)), ..., \text{Var}(\hat{\boldsymbol{\delta}}(x_M^*))\}$. Therefore, $\boldsymbol{z}^{(s)}$ follows a multivariate normal distribution with mean zero, and covariance matrix $\boldsymbol{F}\boldsymbol{\Sigma}_{\hat{\boldsymbol{\delta}}}\boldsymbol{F}^\top$. Since the correlations between test statistics are ignorable in our problem, we adopt the method in Efron (2004, 2007) and Efron (2012) to tackle the correlations in multiple testing.

Given the null hypothesis in (11), controlling the FWER under the significant level α is equivalent to find a threshold c_m, such that

$$\begin{aligned}\sum_{j=1}^{M}P(E_j\ |H_{0j}) &= \text{Prob(at least one } H_j \text{ reject}|\ H_0)\\ &= \text{Prob}(\max\{|z_j^{(s)}|\} > c_m|\ H_0)\\ &= 1 - \text{Prob}(|z_1^{(s)}| \le c_m, |z_2^{(s)}| \le c_m, ..., |z_M^{(s)}| \le c_m|\ H_0)\\ &= 1 - \int_{-c_m}^{c_m}...\int_{-c_m}^{c_m}f(\boldsymbol{z}^{(s)})dz_1^{(s)}dz_2^{(s)}...dz_M^{(s)} = \alpha\end{aligned} \quad (13)$$

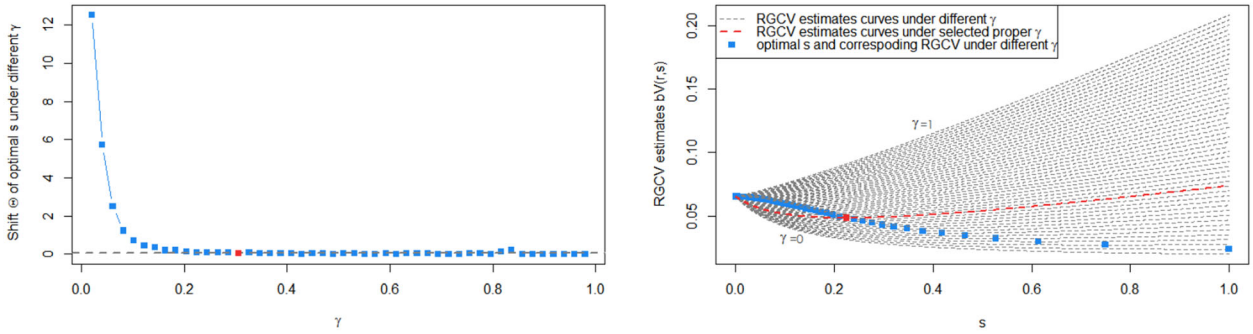

(a) $\boldsymbol{\Theta}(k)$ decreases with $\gamma(k)$. When $\boldsymbol{\Theta}(k) < \theta$, the selected γ is the red dot. The dashed line indicates the threshold $\boldsymbol{\Theta} = \theta$.

(b) Different RGCV paths versus the value of s; from top to bottom, the paths are associated with the values of γ from 1 to 0; the optimal s, denoted by blue dots, can be found at the lowest point on the RGCV path. Red dashed lines represent the RGCV path with respect to the selected γ.

Figure 4. An illustration of auto-selection of RGCV parameters.

Table 1. The specified parameters of the 3D printer for our experiments.

Print Technology	Fused Filament Fabrication
Build Volume	24.6cm Width 16.3 cm Length 15.5 cm Height
Layer Height Settings	High 100 Microns Medium 200 Microns Low 300 Microns
Positioning Precision	XY: 11 microns Z: 2.5 microns
Filament	ABS or PLA Plastic
Filament Diameter	1.75mm
Nozzle Diameter	0.4mm
File Types	STL, OBJ, Thing

where $f(\boldsymbol{z}^{(s)})$ is the probability density function of $\boldsymbol{z}^{(s)}$. For small M, the threshold c_m can be calculated using the exact distribution of the maximum value of correlated random variables as in Arellano-Valle and Genton (2008). However, solving the explicit integral expression under extreme high dimension (i.e., in our case study, $\boldsymbol{z}$ contains 2500 entries) is nearly impossible. Hence, we adopt the integral transformation proposed by Genz (1992) and use numerical Monte Carlo method to find the threshold c_m.

The smoothed test statistics $\boldsymbol{z}^{(s)}$ for the hypothesis in (11) directly assess the local quality of 3D printing surface. In quality characterization, it is often desired to obtain quality measures bounded between 0 and 1. Therefore, we transfer $\boldsymbol{z}^{(s)}$ into p-values to meet with this requirement. Based on c_m, the adjusted p value or scaled local quality measure can be expressed by

$$q_j = q(\beta_1,\beta_2,\beta_3;|z_j^{(s)}|) = \beta_1 - \beta_2 e^{-\beta_3|z_j^{(s)}|^2} \text{ for } j=1,2,\ldots,M \tag{14}$$

where β_1,β_2,β_3 can be found by three constraints: (1) $q_j = 1$ when $|z_j^{(s)}|=0$; (2) $q_j = 0$ when $|z_j^{(s)}|\to\infty$; and (3) $q_j=0.05$ when $|z_j^{(s)}|=c_m$. It is easy to obtain that $\beta_1=0,\beta_2=-1$ and $\beta_3=-\log(\alpha)/c_m^2$. Then we express $q_j=\alpha^{(z_j^{(s)})^2/c_m^2}$ as the scaled quality measure on test site j.

Case study I

This section provides a case study to show that the proposed approach can effectively assess the local quality of 3D printing surfaces.

Experimental setting

The 3D printing datasets with respect to the designed surface $y_d(\boldsymbol{x})$ and the printed object $y_p(\boldsymbol{x})$ are collected from two different mechanisms. Specifically, the designed surface is constructed through 3D Computer-Aided Design (CAD) in Rhinoceros 5 SR14 64-bit (version 5.14.522.8390), whereas the data points in the printed object are obtained from a 3D laser scanning equipment.

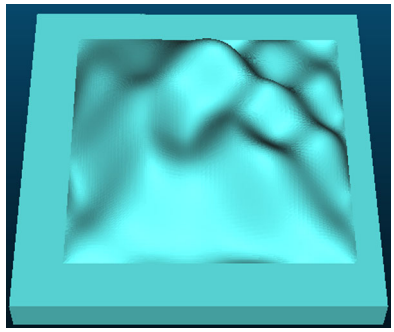

Figure 5. Original CAD models of the surface.

The laser scanner used for surface measurement is of a precision equal to 0.05 mm. For registration, we adopt the iterative closest point (ICP), a wide-used method for the accurate and computationally efficient registration of 3D shapes (Besl and McKay 1992; Zhang 1994). During this process, the registration error decreases. Generally, after some iterations, the square root difference between two iterations becomes lower than a given threshold, then the iteration is terminated. We also adopt ICP as a registration tool in the following research. The registration errors in our case studies are control by a root mean square less than 0.08 mm.

The 3D printer used in this study is the Makerbot Replicator 2X desktop. Poly-lactic acid (PLA) is used as the printing material. This material has good mechanical properties and is eco-friendliness (Jo et al. 2012). The printer uses Fused Deposition Modeling (FDM) technology (Gibson et al. 2010; Guo and Leu 2013) to form the products. A thread of a plastic filament is heated and adhered to a substrate before it is solidified. In this way, a new layer is formed gradually. The layer height and the infill proportion can be adjusted according to the required precision level. The specified parameters of the printer are provided in Table 1. The size of the printed object in our experiment is 49 mm × 49 mm with a 63 mm × 63 mm square bottom, as illustrated in Figure 5. The unit of the surface topography is millimeter in this paper.

Our experiment is described as follows. We first print a 3D surface under a lower precision with layer height equal to 0.3 mm and the infill parameter equal to 10%. This printed object is referred to as $\boldsymbol{S}_1$ hereafter. Note that the geometric deformation is reproducible. We print three copies of the same 3D surface,

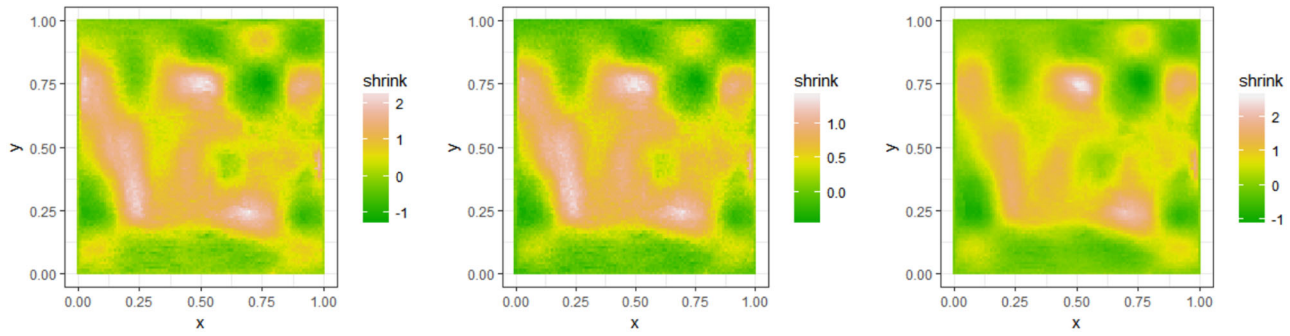

(a) Measured shrinkage of $\boldsymbol{S}_{1,a}$ (b) Measured shrinkage of $\boldsymbol{S}_{1,b}$ (c) Measured shrinkage of $\boldsymbol{S}_{1,c}$

Figure 6. Three replicates of $\boldsymbol{S}_1$.

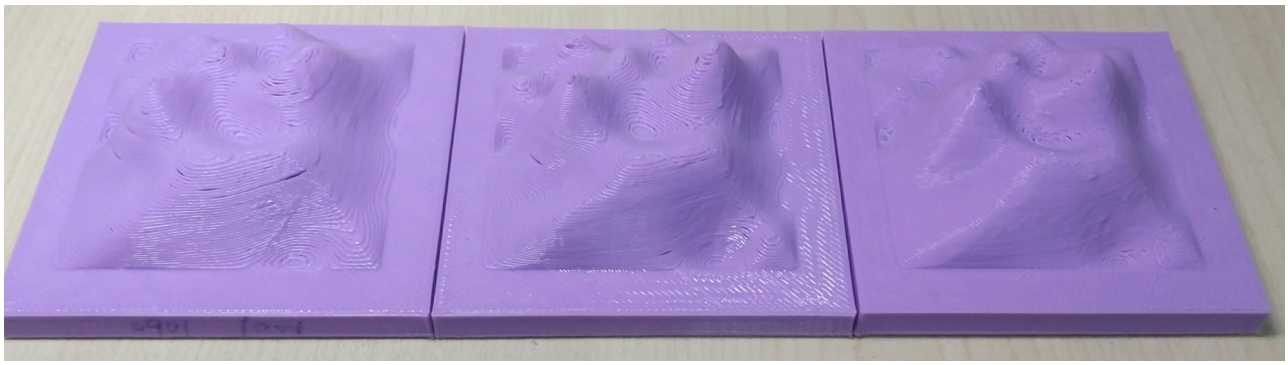

Figure 7. Picture of printed object $\boldsymbol{S}_1$(left), $\boldsymbol{S}_2$(middle) and $\boldsymbol{S}_3$(right).

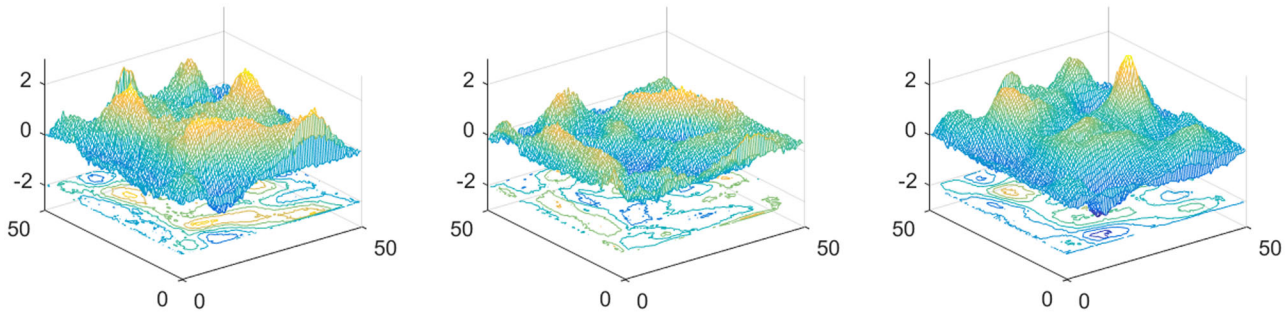

(a) $\delta(\mathbf{x})$ of $\mathbf{S}_1$ (b) $\delta(\mathbf{x})$ of $\mathbf{S}_2$ (c) $\delta(\mathbf{x})$ of $\mathbf{S}_3$

Figure 8. Deformation $\delta(\boldsymbol{x})$ of the three surfaces.

i.e., $\boldsymbol{S}_{1,a}$ and $\boldsymbol{S}_{1,b}$ and $\boldsymbol{S}_{1,c}$ are three printed objects of $\boldsymbol{S}_1$. The measured deviations are shown in Figure 6. They all suffer from severer shrinkage in some steep areas of the design surface. It validates that, under same machine settings, the deformations of the printed objects resemble each other, and the corresponding compensation design should be relatively stable across different replications under a fix machine setting. The reason is that, an object using the same machine, the same material, and the same printer-supported document, nearly all the inaccuracy causes during the preprocess (such as format converting errors), in-process (such as the positioning capability, temperature controlling) and post-process (such as contraction with cold and residual stress-induced distortion) are repeatable. Therefore, the warping and deformation due to these reasons should share same characters in the next print cycling. In the rest of this case study, we focus on discussing the results from the first replicates, i.e., $\boldsymbol{S}_{1,a}$.

According to the characterization results of $\boldsymbol{S}_{1,a}$ (denoted by $\boldsymbol{S}_1$ in the following), we adopt a minimum squared distance optimization method on the y-axis to compensate the original design. That is, we supplement the original CAD model from the y-axis according to the measured shrinkage values to

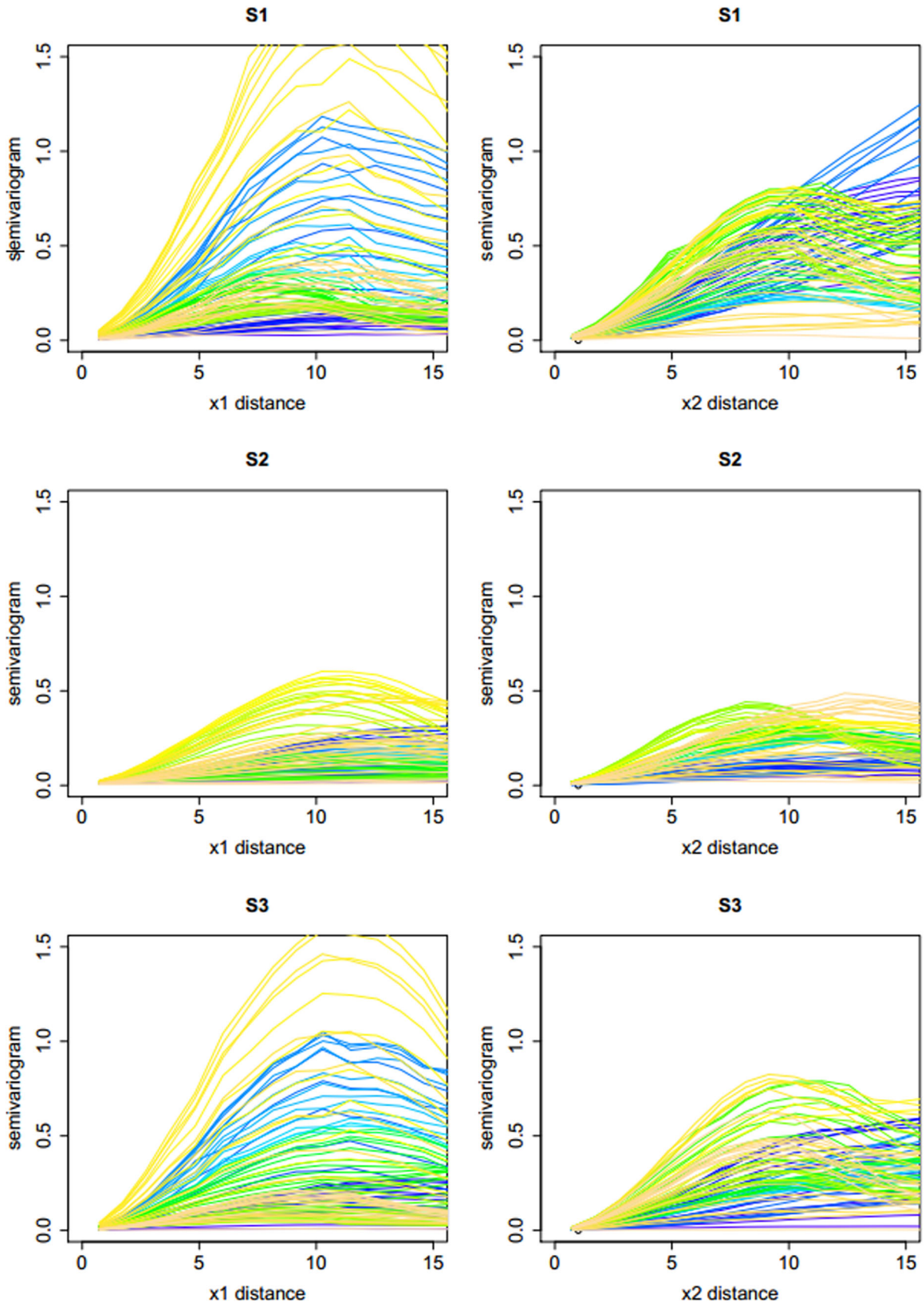

Figure 9. Semi-variogram plots along x_1 and x_2 directions from S_1 (top panel), S_2 (middle panel) and S_3 (bottom panel).

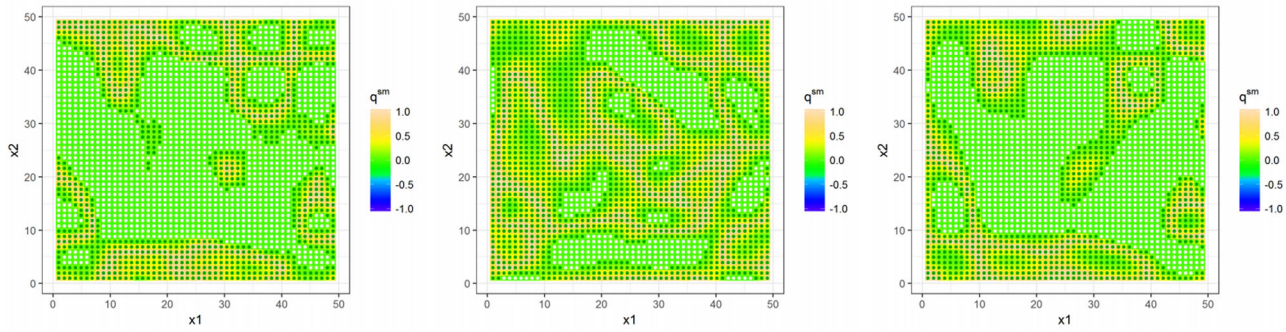

(a) $\boldsymbol{q}^{sm}$ of $\boldsymbol{S}_1$ (b) $\boldsymbol{q}^{sm}$ of $\boldsymbol{S}_2$ (c) $\boldsymbol{q}^{sm}$ of $\boldsymbol{S}_3$

Figure 10. Quality measure $\boldsymbol{q}^{sm}$ with significant marker, adopting proposed adaptive RGCV smoothing method to $\boldsymbol{z}$.

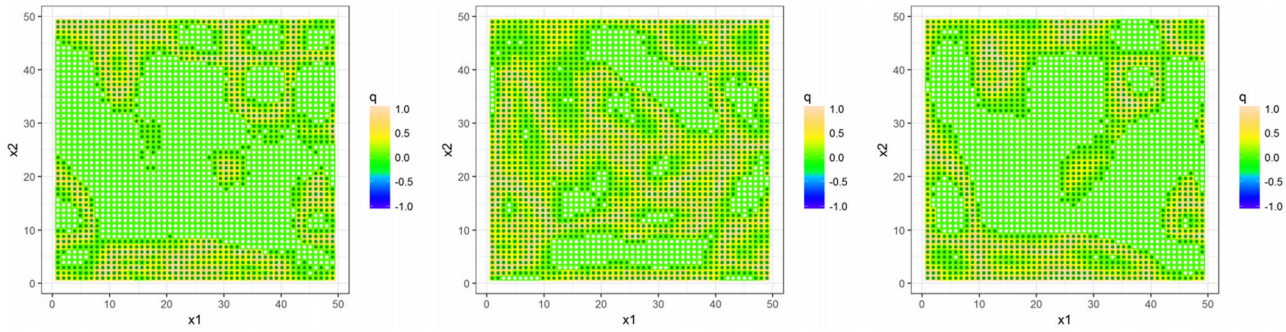

(a) $\boldsymbol{q}$ of $\boldsymbol{S}_1$ (b) $\boldsymbol{q}$ of $\boldsymbol{S}_2$ (c) $\boldsymbol{q}$ of $\boldsymbol{S}_3$

Figure 11. Direct quality measure $\boldsymbol{q}$ from $\boldsymbol{z}$, do not apply any smoothing.

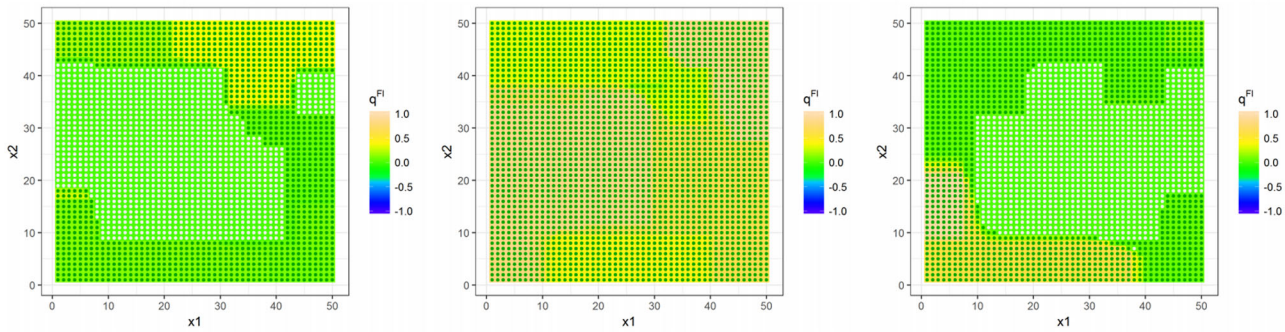

(a) $\boldsymbol{q}^{Fl}$ of $\boldsymbol{S}_1$ (b) $\boldsymbol{q}^{Fl}$ of $\boldsymbol{S}_2$ (c) $\boldsymbol{q}^{Fl}$ of $\boldsymbol{S}_3$

Figure 12. Quality measure $\boldsymbol{q}^{Fl}$ with significant marker, adopting fused lasso method to $\boldsymbol{z}$ as a benchmark.

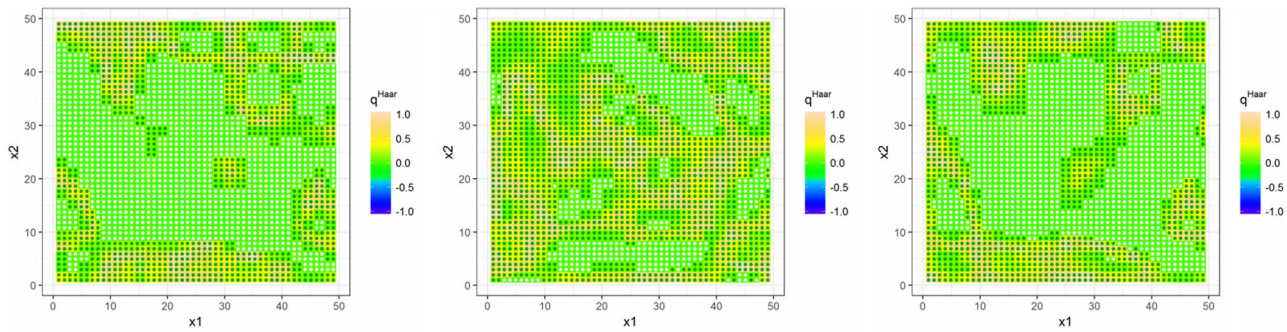

(a) $\boldsymbol{q}^{Haar}$ of $\boldsymbol{S}_1$ (b) $\boldsymbol{q}^{Haar}$ of $\boldsymbol{S}_2$ (c) $\boldsymbol{q}^{Haar}$ of $\boldsymbol{S}_3$

Figure 13. Quality measure $\boldsymbol{q}^{Haar}$ with significant marker, adopting 2D Haar wavelet to $\boldsymbol{z}$ as a benchmark.

generate the compensated surface, denoted by S_2. For comparison purpose, the same surface is also printed under a higher precision setting with layer height equals to 0.1 mm and the infill parameter equals to 20%. The printed object under this high precision is referred to as S_3. Our analysis is based on the three surfaces, which is shown in Figure 7. For each printed object, the measured domain contains 10000 points, and the test domain is a 50×50 regular grid.

Experimental results

We assess the dimensional accuracy on the test location and characterize their quality for the three surfaces as shown in Figure 7. Figure 8 plots the original measured deformation surfaces, i.e., $\delta(\boldsymbol{x})$ in Eq. (1). To validate the covariance function in (3), we report in Figure 9 the semi-variogram plots along x_1 and x_2 directions of S_1 - S_3. The figure shows that the separable covariance structure appears to be a reasonable assumption for our experiments.

Figure 10 reports the final quality measure with significant marker, after adopting our proposed adaptive RGCV smoothing method to $\boldsymbol{z}$. The quality measures can directly indicate low quality locations. In Figure 11, the low quality and high quality areas are displayed by green and pink spots on the test locations. The assessment result shows that, for S_2, the dimensional deviation is not significant in most areas. Compared with S_2, S_1 and S_3 contain significant local quality issues due to dimensional deviation. Besides, the heat maps of the scaled quality measure $\boldsymbol{q}$ provide a direct quality assessment within the region of interests. By comparing the quality measures, our method can effectively identify the quality difference between the printed objects under low precision setting and high precision setting. Also, by comparing the quality of S_1 and S_2, the quality of S_2 is significantly improved after compensation. It is seen that the quality of compensated low precision surface S_2 is better than the quality of the high precision surface S_3 without compensation.

To better evaluate the performance of the proposed method, we consider two benchmark methods based on Tibshirani and Taylor (2011) and Fu, Muralikrishnan, and Raja (2003). Tibshirani and Taylor (2011) considered the 2D fused lasso method in spatial (and image) data, while Fu, Muralikrishnan, and Raja (2003) adopt wavelet method to extract the roughness of engineering surfaces. These two approaches will be used as alternatives of our proposed RGCV method with L_2 smoothness penalty to process the original z statistics in Section "Quality

Table 2. The global quality measures in (15) associated with the surface quality measures in Figures 10–13.

	$\bar{q}_{\mathcal{P}_M}$		
Methods	S_1	S_2	S_3
q^{sm} (proposed)	0.1906	0.3450	0.1971
q	0.1899	0.3388	0.1988
q^{Fl}	0.0648	0.6371	0.1080
q^{Haar}	0.1882	0.3453	0.1969

Table 3. The global quality measure in the test domain for the three repeatedly printed objects before compensatory adjustment (denoted by S_4) and the corresponding compensated surfaces after compensatory adjustment (denoted by S_5).

	$\bar{q}_{\mathcal{P}_M}$	
Replication	S_4	S_5
1	0.4648	0.8723
2	0.2383	0.9404
3	0.5023	0.9010

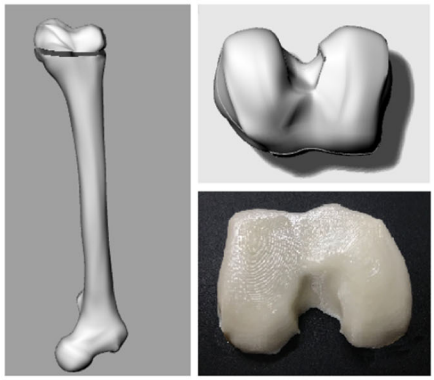

(a) The femur model (left), the part to be printed (upper-right) and one of the printed objects (bottom-right).

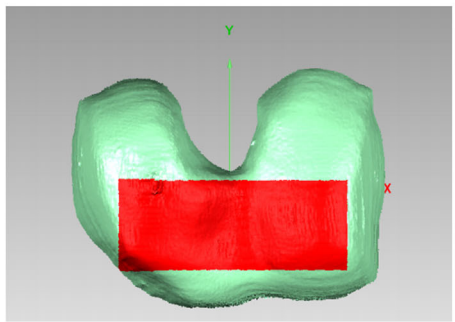

(b) The test domain marked by red where we conduct quality assessment.

Figure 14. The Design model, the picture of printed objects and the assessment domain.

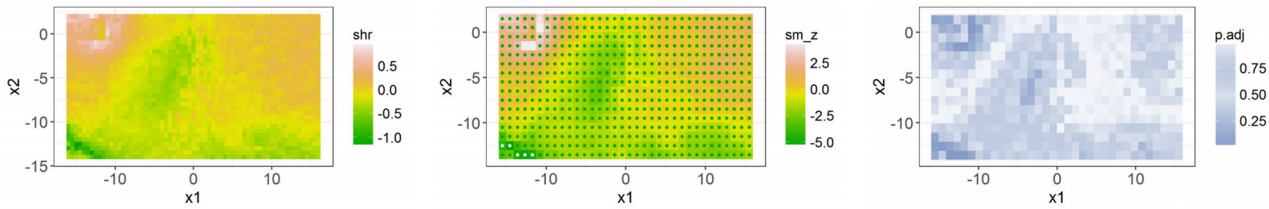

(a) Deformation surface $\delta(\boldsymbol{x})$ from $\boldsymbol{S_4}$. (b) $\boldsymbol{z}^{(s)}$ from $\boldsymbol{S_4}$. (c) $\boldsymbol{q}$ from $\boldsymbol{S_4}$.

Figure 15. Quality evaluation results from the printed object without compensatory adjustment.

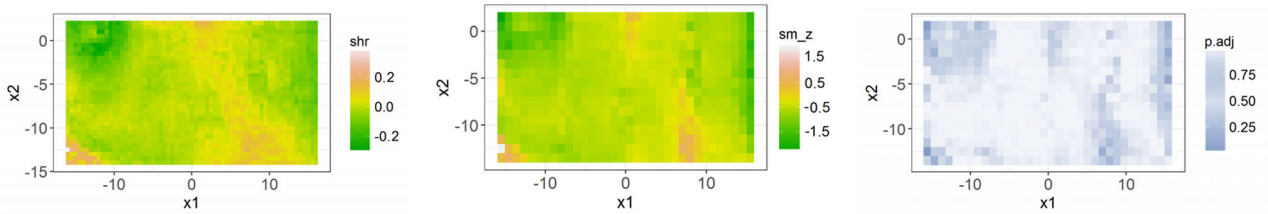

(a) Deformation surface $\delta(\boldsymbol{x})$ from $\boldsymbol{S_4}$. (b) $\boldsymbol{z}^{(s)}$ from $\boldsymbol{S_4}$. (c) $\boldsymbol{q}$ from $\boldsymbol{S_4}$.

Figure 16. Quality evaluation results from the printed object with compensatory adjustment.

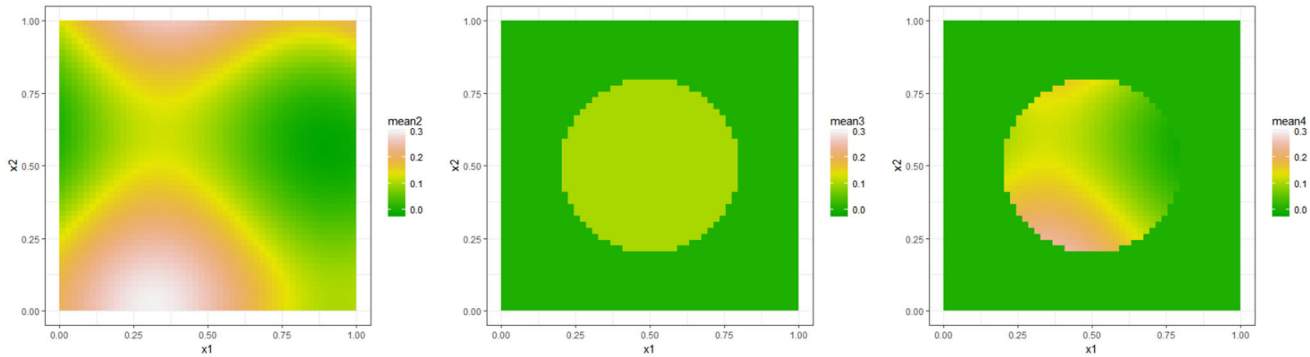

(a) Scheme (i) (b) Scheme (ii) (c) Scheme (iii)

Figure 17. The three types of deformation in simulation studies.

assessment and characterization." Note that in the fields of 3D printing free-form surfaces, we have not found direct comparable method in the literature. The dimensional quality evaluation is usually terminated at a deviation estimate on some specific spatial locations, or described as some global indices.

Let us denote $\boldsymbol{q}$ to be the quality results generated from the original $\boldsymbol{z}$ statistics. The quality results generated from our proposed method are denoted by $\boldsymbol{q}^{sm}$. By adopting the 2D fused lasso method to the original $\boldsymbol{z}$ statistics, we obtain a spatial fused statistic $\boldsymbol{z}^{Fl}$ before generating quality measure $\boldsymbol{q}^{Fl}$. By adopting the 2D Haar wavelet method to the original $\boldsymbol{z}$ statistics, we obtain a filtered statistic $\boldsymbol{z}^{Haar}$ before generating quality measure $\boldsymbol{q}^{Haar}$. Figure 11–13 illustrate the quality results of $\boldsymbol{q}^{Fl}, \boldsymbol{q}^{Haar}, \boldsymbol{q}$ and $\boldsymbol{q}^{sm}$. A metric $\bar{q}_{\mathcal{P}_\mathcal{M}}$ is used to provide a global quality measure by summarizing the local quality in the test domain $\mathcal{P}_\mathcal{M}$:

$$\bar{q}_{\mathcal{P}_\mathcal{M}} = \frac{\sum_{i=1}^{M} q_i}{M}. \tag{15}$$

The global quality measures associated with Figures 10–13 are given in Table 2. Same as the original local quality measure, the global quality measure ranges from 0–1 with 0 demonstrating low quality and 1 demonstrating high quality. Table 2 shows consistent assessment results of the three surfaces from different methods.

From Figure 11, it is seen that, without smoothing of $\boldsymbol{z}$, the significant low quality areas contain a large amount of noise, and there are many discrete significant locations. However, when adopting fused lasso method in Figure 12, many nearby locations are forced to have equivalent quality measures. The significant areas can no longer reflect the original quality information. From Figure 13, it appears that Haar

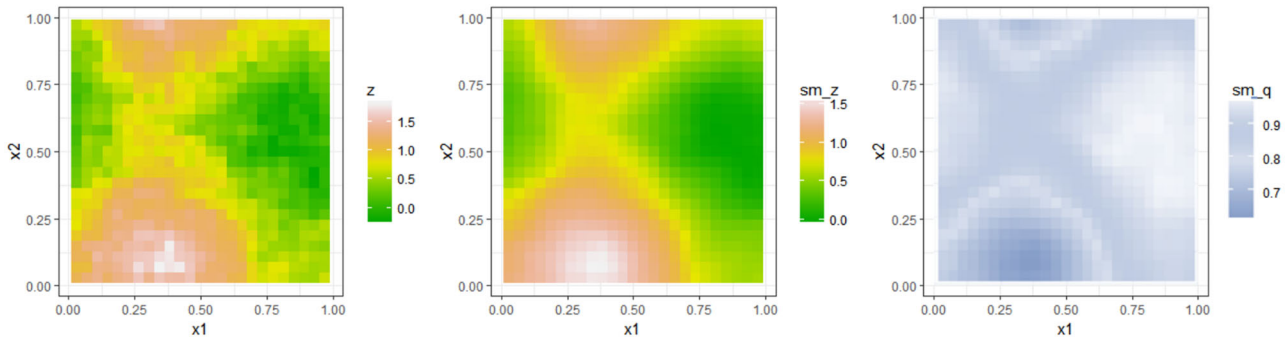

(a) Deformation scheme (i): unsmoothed $\boldsymbol{z}$ (left), $\boldsymbol{z}^{(s)}$ (middle), and scaled quality $\boldsymbol{q}$ (right).

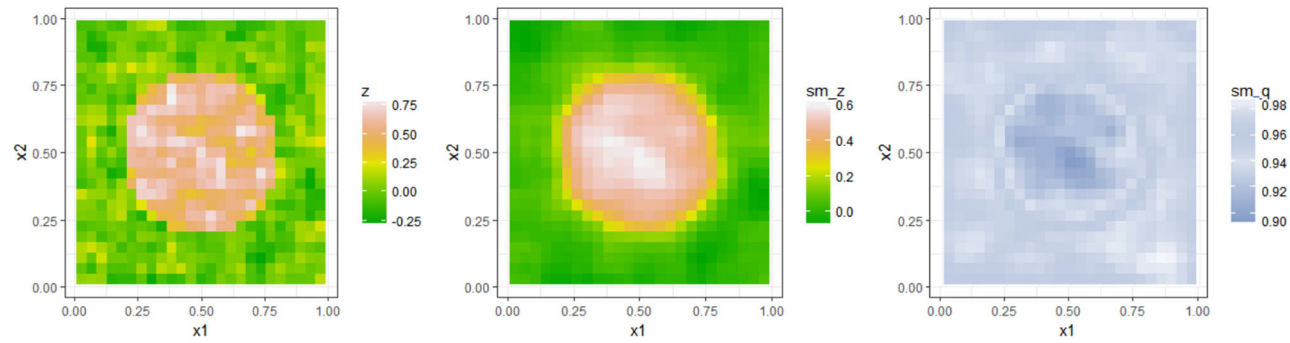

(b) Deformation scheme (ii): unsmoothed $\boldsymbol{z}$ (left), $\boldsymbol{z}^{(s)}$ (middle), and scaled quality $\boldsymbol{q}$ (right).

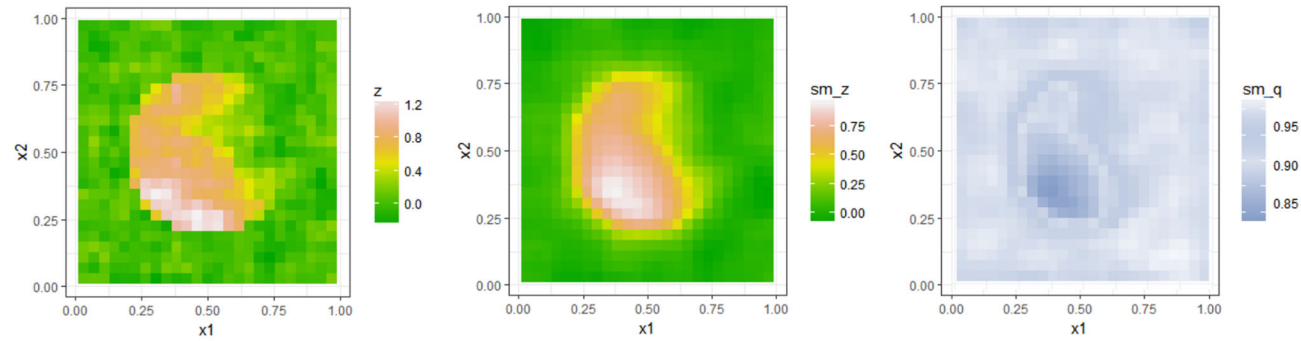

(c) Deformation scheme (iii): unsmoothed $\boldsymbol{z}$ (left), $\boldsymbol{z}^{(s)}$ (middle), and scaled quality $\boldsymbol{q}$ (right).

Figure 18. Average results of 100 replications under $\theta_1 = \theta_2 = 25$ and $\sigma^2 = 0.04$ on three types of deformation.

wavelet method performs better than fused lasso method. But it still cannot formulate smooth boundary as our proposed method in Figure 10. Compared with benchmark methods, the proposed quality assessment scheme can provide more accurate local quality measures.

Case study II

In this section, we provide another case study based on a bio-medical application to show that the proposed scheme can deal with complex applications. This case study comes from the 3D printing of a human femur malleolus. Here the printed object can be used as part of the navigation plates in the surgery, so it is critically important to control the deformations.

As shown in Figure 14a, after designating a reference plane, we still adopt the Cartesian coordinates system (x_1, x_2, y) to characterize the geometric shape of the 3D design. Based on previous practices, we designate a critical area as the test domain on the surface, shown in Figure 14b. The dimension deviation quality of the surface are characterized on a 48×16 regular grid.

In this study, we compare the dimensional quality before and after applying the compensatory adjustment based on the measured deviation. The assessment surface before compensatory is referred to as $\boldsymbol{S_4}$, whereas the surface after compensatory is referred to as $\boldsymbol{S_5}$. They are printed under the same precision with layer height equal to 0.2 mm and the infill parameter equal to 15%. The printer is the same as the one in

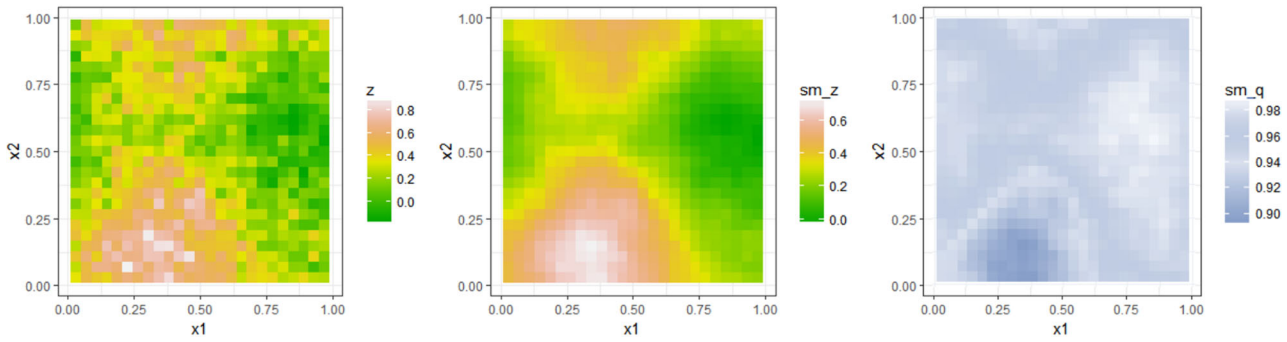

(a) Deformation scheme (i): unsmoothed $\boldsymbol{z}$ (left), $\boldsymbol{z}^{(s)}$ (middle), and scaled quality $\boldsymbol{q}$ (right).

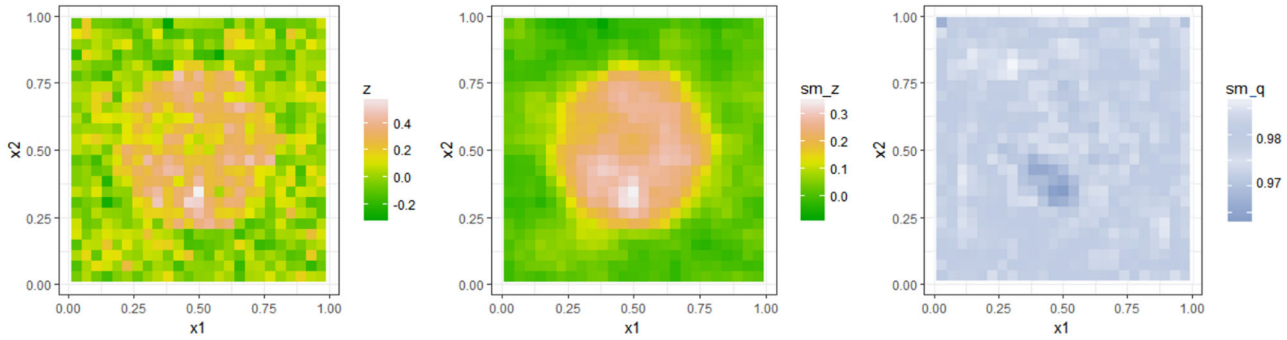

(b) Deformation scheme (ii): unsmoothed $\boldsymbol{z}$ (left), $\boldsymbol{z}^{(s)}$ (middle), and scaled quality $\boldsymbol{q}$ (right).

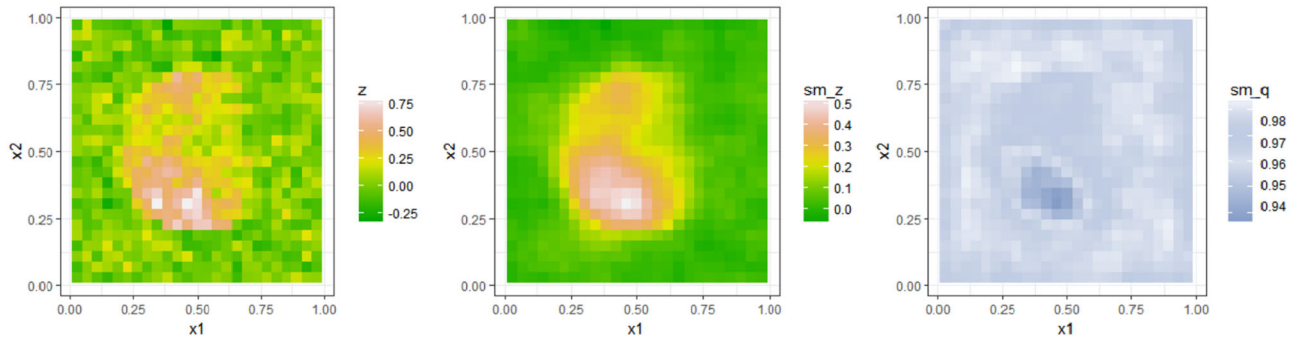

(c) Deformation scheme (iii): unsmoothed $\boldsymbol{z}$ (left), $\boldsymbol{z}^{(s)}$ (middle), and scaled quality $\boldsymbol{q}$ (right).

Figure 19. Average results of 100 replications under $\theta_1 = \theta_2 = 73$ and $\sigma^2 = 0.15$ on three types of deformation.

the previous case study. Acrylonitrile-butadine-styrene (ABS) is used as the printing material. We perform multiple repetitions for this experiment. The global quality measures in (15) are provided in Table 3. We find that after adopting a compensatory adjustment, the overall quality has been significantly improved.

Besides the above global metric, here we use the first replication as an example to visualize results of our dimension deviation quality characterization. Figure 15 depicts the quality measures of $\boldsymbol{S_4}$ without compensatory adjustment. Figure 16 provides the corresponding results of $\boldsymbol{S_5}$ after adopting a compensatory adjustment. Using the same printing precision as before, the dimensional accuracy of the compensatory adjusted object is significantly improved. The results demonstrate that, the proposed procedures are effective for characterizing dimensional deviations in this bio-medical application.

Simulation study

This section evaluates the impact of smoothing original z-statistics before quality assessment. Simulation experiments are provided based on synthetic data with different levels of overall variance (σ^2) and spatial dependence ($\boldsymbol{\theta}$). Without loss of generality, we directly generate the deformation surface $\delta(\boldsymbol{x})$ as a realization of Gaussian process with mean function $\mu(\boldsymbol{x})$ and covariance function $\text{cov}(\boldsymbol{x}_1, \boldsymbol{x}_2) = \sigma^2 \exp\{-\theta_1|x_{11} - x_{21}| - \theta_2|x_{12} - x_{22}|\}$. The mean function $\mu(\boldsymbol{x})$ are generated

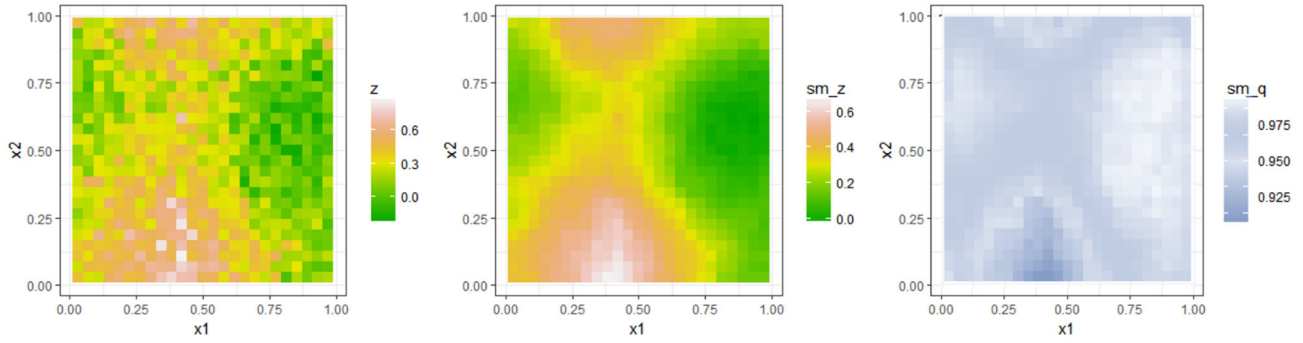

(a) Deformation scheme (i): unsmoothed $\boldsymbol{z}$ (left), $\boldsymbol{z}^{(s)}$ (middle), and scaled quality $\boldsymbol{q}$ (right).

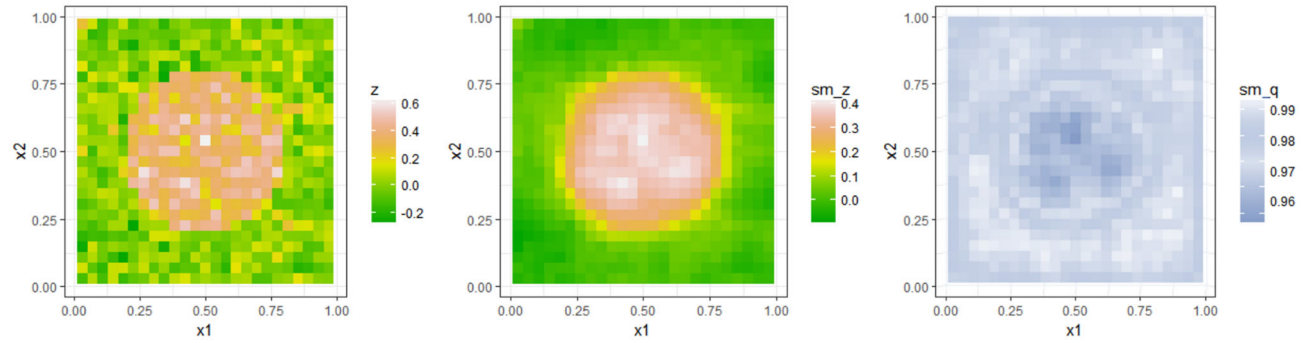

(b) Deformation scheme (ii): unsmoothed $\boldsymbol{z}$ (left), $\boldsymbol{z}^{(s)}$ (middle), and scaled quality $\boldsymbol{q}$ (right).

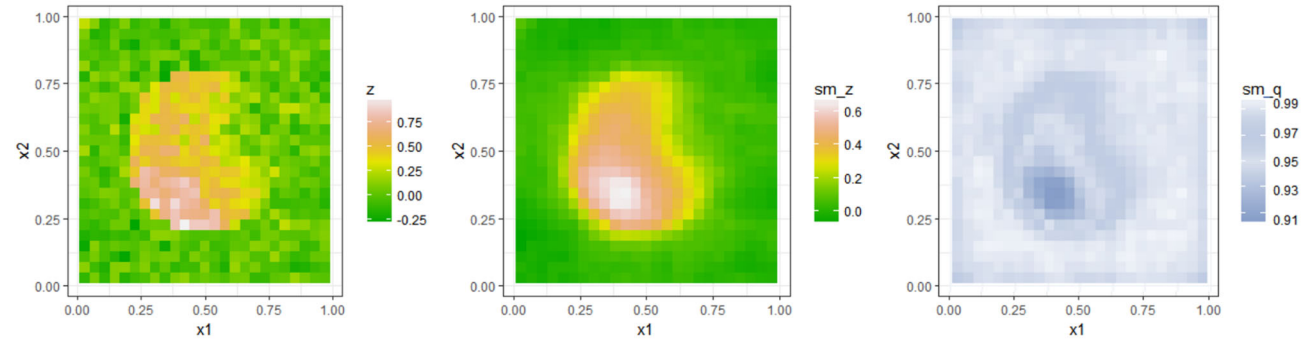

(c) Deformation scheme (iii): unsmoothed $\boldsymbol{z}$ (left), $\boldsymbol{z}^{(s)}$ (middle), and scaled quality $\boldsymbol{q}$ (right).

Figure 20. Average results of 100 replications under $\theta_1 = \theta_2 = 49$ and $\sigma^2 = 0.26$ on three types of deformation.

under three different schemes: (a) continuous, $\mu(\boldsymbol{x}) = 0.1(\sin(5x_1) + \cos(5x_2) + 2\exp(x_1x_2))$; (b) discrete, $\mu(\boldsymbol{x}) = 0.1I((x_1 - 1/2)^2 + (x_2 - 1/2)^2 < 0.3)$; (c) combination, $\mu(\boldsymbol{x}) = 0.1(\sin(5x_1) + \cos(5x_2) + 2\exp(x_1x_2))\ I((x_1 - 1/2)^2 + (x_2 - 1/2)^2 < 0.3)$. The three types of deformation are depicted in Figure 17.

Given the Gaussian process parameters (θ_1, θ_2) and σ^2, we generate 100 realizations of the deformation surface $\delta(\boldsymbol{x})$, and calculate the local quality statistics $\boldsymbol{z}^{(s)}$ and quality measure $\boldsymbol{q}$ for each realization. The deformation surface $\delta(\boldsymbol{x})$ is generated on a 50×50 grid, and evaluated on a 25×25 test domain. We use average results to summarize the testing power and the assessment results.

Figures 18–20 provide the quality assessment results for the three schemes under three different parameter settings of the Gaussian process parameters (θ_1, θ_2) and σ^2, respectively. Particularly, $\theta_1 = \theta_2 = 25$ and $\sigma^2 = 0.04$ in Figure 18, $\theta_1 = \theta_2 = 73$ and $\sigma^2 = 0.15$ in Figure 19, and $\theta_1 = \theta_2 = 49$ and $\sigma^2 = 0.26$ in Figure 20. Notice that $\boldsymbol{\theta}$ is associated with the strength of spatial correlation, and σ^2 is associated with the overall variation level. Figure 18 represents the results when the noise level is relatively low. The left penal in Figure 18 show that the un-smoothed $\boldsymbol{z}$ values are noisy over the test domain. As the variation increase, Figures 19 and 20 show that the un-smoothed results become more unstable. After smoothing the original $\boldsymbol{z}$-statistic, the noise in $\boldsymbol{z}$ values is

removed while the shapes and characters of the deformation are clearly presented. The smoothed $\boldsymbol{z}^{(s)}$ statistics and the scaled quality measures $\boldsymbol{q}$ effectively recover the underlying noises in the assessment process.

Discussion

In this work, we propose a statistics-guided approach for characterizing free-form surfaces, especially in the application to 3D printing objects with continuous surface based on 3D scanning data. The proposed method contains two key steps: a Gaussian process model is used to interpolate the dimensional deviation on the test domain for generating test statistics $\boldsymbol{z}$, and a spatial second-order difference penalty approach is developed to smooth the original quality test statistics $\boldsymbol{z}$. The quality assessment scheme generates continuous significant and insignificant areas. The scaled quality measure $\boldsymbol{q}$ provides direct quality viewing among different objects. The case study shows that the proposed procedures are effective for assessing dimensional quality.

We remark that the proposed quality assessment procedure can be implemented efficiently in terms of computational efforts. The proposed method can be easily extended to quality assessment in some critical areas by constructing test domains and designating weights to emphasize on the evaluation of those critical areas. Moreover, this framework provides good tolerance to the different kinds of deformation process, since the spatial dependence of the deformation is inevitable. This work also provides reasonable quality assessment across different surfaces. Though customized designs are different in geometrical dimensions and the scanned equipment may export point cloud data with different densities and measurement errors, the test procedures can provide comparable assessments.

It should be noted that, in this research we use height to evaluate the dimension deviation, which is explicit and convenient. Though this proposed method can be applied to some other scenarios, it cannot be directly applied to all kinds of 3D geometries. There are limitations and challenges imposed by actual 3D geometries, which can be our further research direction. Beside, the use of Gaussian process (GP) needs a careful examination on its model assumption. As a promising future direction, this issue can also be addressed by adopting other flexible smoothing methods (Yang and Qiu 2018, 2019).

About the authors

Hao Wang is currently working toward a PhD degree in the Department of Industrial Engineering, Tsinghua University, Beijing, China. She received the BS degree from Tianjin University, Tianjin, China, in 2010. Her general research interests include statistical modeling, process monitoring in manufacturing processes. Ms. Wang is a member of the Institute for Operations Research and the Management Sciences (INFORMS).

Qiong Zhang is an Assistant Professor in Statistics at Clemson University. She holds PhD degree in Statisticsfrom the University of Wisconsin- Madison. Her research interests include design and analysis for computer experiments, uncertainty quantification, and statistical methods in Engineering. She is a member of ASA and INFORMS.

Kaibo Wang is Professor in the Department of Industrial Engineering, Tsinghua University, Beijing, China. He received his BEng, and MS degrees in Mechatronics and Mechanical Engineering from Xi'an Jiaotong University, Xi'an, China, in 1999 and 2002 respectively, and PhD in Industrial Engineering and Engineering Management from Hong Kong University of Science and Technology, Hong Kong, in 2006. His research focuses on statistical quality control and data-driven system modelling, monitoring, diagnosis and control, with a special emphasis on the integration of engineering knowledge and statistical theories for solving problems from the real industry. He has published more than 40 peer reviewed papers in journals such as *Journal of Quality Technology, IISE Transactions, Quality and Reliability Engineering International, IEEE Transactions on Automation Science and Engineering*, and others.

Xinwei Deng is an associate professor in the Department of Statistics at Virginia Tech. He received his PhD from Georgia Institute of Technology in 2009. Dr. Deng's research interests include data analytics, machine learning, design of experiments, and interface between experimental design and machine learning. Dr. Deng actively collaborates with researchers in engineering, nanotechnology, bioinformatics, and environmental sciences. He has over 50 peer-reviewed top journal and conference publications.

Acknowledgments

The authors thank the editor, and two referees for their helpful comments and suggestions, which have led to improvements in the article.

Funding

Miss Hao Wang and Dr. Kaibo Wang's work are supported by the Key Program of the National Natural Science Foundation of China (Grant No. 71932006 and 71731008).

ORCID

Qiong Zhang http://orcid.org/0000-0003-1995-2127
Kaibo Wang http://orcid.org/0000-0001-9888-4323
Xinwei Deng http://orcid.org/0000-0002-1560-2405

References

Ameta, G., R. Lipman, S. Moylan, and P. Witherell. 2015. Investigating the role of geometric dimensioning and

tolerancing in additive manufacturing. *Journal of Mechanical Design* 137 (11):111401. doi:10.1115/1.4031296.

Arellano-Valle, R. B., and M. G. Genton. 2008. On the exact distribution of the maximum of absolutely continuous dependent random variables. *Statistics & Probability Letters* 78 (1):27–35. doi:10.1016/j.spl.2007.04.021.

Armillotta, A. 2006. Assessment of surface quality on textured fdm prototypes. *Rapid Prototyping Journal* 12 (1): 35–41. doi:10.1108/13552540610637255.

Babu, M., P. Franciosa, and D. Ceglarek. 2019. Spatio-temporal adaptive sampling for effective coverage measurement planning during quality inspection of free form surfaces using robotic 3d optical scanner. *Journal of Manufacturing Systems* 53:93–108. doi:10.1016/j.jmsy.2019.08.003.

Bayarri, M. J., J. O. Berger, R. Paulo, J. Sacks, J. A. Cafeo, J. Cavendish, C.-H. Lin, and J. Tu. 2007. A framework for validation of computer models. *Technometrics* 49 (2): 138–54. doi:10.1198/004017007000000092.

Besl, P. J., and N. D. McKay. 1992. Method for registration of 3-d shapes. *Sensor Fusion IV: Control Paradigms and Data Structures* 1611:586–606. In volume International Society for Optics and Photonics.

Cassetta, M., L. V. Stefanelli, M. Giansanti, and S. Calasso. 2012. Accuracy of implant placement with a stereolithographic surgical template. *International Journal of Oral & Maxillofacial Implants* 27 (3):655–663.

Chen, H., D. Wu, H. Yang, and K. Guo. 2015. Clinical use of 3D printing guide plate in posterior lumbar pedicle screw fixation. *Medical Science Monitor* 21:3948–54. doi: 10.12659/MSM.895597.

Desta, M. T., H. Feng, and D. Ouyang. 2003. Characterization of general systematic form errors for circular features. *International Journal of Machine Tools and Manufacture* 43 (11):1069–78. doi:10.1016/S0890-6955(03)00128-7.

Diblasi, A., and A. Bowman. 2001. On the use of the variogram in checking for independence in spatial data. *Biometrics* 57 (1):211–8. doi:10.1111/j.0006-341X.2001.00211.x.

Efron, B. 2004. Large-scale simultaneous hypothesis testing: The choice of a null hypothesis. *Journal of the American Statistical Association* 99 (465):96–104. doi:10.1198/016214504000000089.

Efron, B. 2007. Correlation and large-scale simultaneous significance testing. *Journal of the American Statistical Association* 102 (477):93–103. doi:10.1198/016214506000001211.

Efron, B. 2012. *Large-scale inference: Empirical Bayes methods for estimation, testing, and prediction*, vol. 1. New York, NY: Cambridge University Press.

Fu, S., B. Muralikrishnan, and J. Raja. 2003. Engineering surface analysis with different wavelet bases. *Journal of Manufacturing Science and Engineering* 125 (4):844–52. doi:10.1115/1.1616947.

Genz, A. 1992. Numerical computation of multivariate normal probabilities. *Journal of Computational and Graphical Statistics* 1 (2):141–9. doi:10.2307/1390838.

Gibson, I., D. W. Rosen, B. Stucker, et al. 2010. *Additive manufacturing technologies*, vol. 238. New York, NY: Springer.

Green, P. J., and B. W. Silverman. 1993. *Nonparametric regression and generalized linear models: A roughness penalty approach*. Baco Raton, FL: Chapman and Hall/CRC.

Guo, N., and M. C. Leu. 2013. Additive manufacturing: Technology, applications and research needs. *Frontiers of Mechanical Engineering* 8 (3):215–43. doi:10.1007/s11465-013-0248-8.

He, J., D. Li, B. Lu, Z. Wang, and T. Zhang. 2006. Custom fabrication of a composite hemi-knee joint based on rapid prototyping. *Rapid Prototyping Journal* 12 (4): 198–205. doi:10.1108/13552540610682705.

Huang, Q. 2016. An analytical foundation for optimal compensation of three-dimensional shape deformation in additive manufacturing. *Journal of Manufacturing Science and Engineering* 138 (6):061010. doi:10.1115/1.4032220.

Jo, M. Y., Y. J. Ryu, J. H. Ko, and J.-S. Yoon. 2012. Effects of compatibilizers on the mechanical properties of abs/pla composites. *Journal of Applied Polymer Science* 125 (S2):E231–E238. doi:10.1002/app.36732.

Krulikowski, A. 1998. *Fundamentals of geometric dimensioning and tolerancing*. Independence, KY: Cengage Learning.

Lasemi, A., D. Xue, and P. Gu. 2010. Recent development in cnc machining of freeform surfaces: A state-of-the-art review. *Computer-Aided Design* 42 (7):641–54. doi:10.1016/j.cad.2010.04.002.

Li, Y., and P. Gu. 2004. Free-form surface inspection techniques state of the art review. *Computer-Aided Design* 36 (13):1395–417. doi:10.1016/j.cad.2004.02.009.

Luan, H., and Q. Huang. 2015. Predictive modeling of in-plane geometric deviation for 3d printed freeform products. In *IEEE Automation Science and Engineering (CASE), 2015 IEEE International Conference on*, 912–7.

Lukas, M. A. 2006. Robust generalized cross-validation for choosing the regularization parameter. *Inverse Problems* 22 (5):1883–902. doi:10.1088/0266-5611/22/5/021.

Maglione, D., and A. Diblasi. 2004. Exploring a valid model for the variogram of an isotropic spatial process. *Stochastic Environmental Research and Risk Assessment* 18 (6):366–76. doi:10.1007/s00477-003-0143-7.

Mahmood, S., A. J. Qureshi, and D. Talamona. 2018. Taguchi based process optimization for dimension and tolerance control for fused deposition modelling. *Additive Manufacturing* 21:183–90. doi:10.1016/j.addma.2018.03.009.

Mazzoni, S., C. Marchetti, R. Sgarzani, R. Cipriani, R. Scotti, and L. Ciocca. 2013. Prosthetically guided maxillofacial surgery: Evaluation of the accuracy of a surgical guide and custom-made bone plate in oncology patients after mandibular reconstruction. *Plastic and Reconstructive Surgery* 131 (6): 1376–85. doi:10.1097/PRS.0b013e31828bd6b0.

Mehra, P., J. Miner, R. D'Innocenzo, and M. Nadershah. 2011. Use of 3-d stereolithographic models in oral and maxillofacial surgery. *Journal of Maxillofacial and Oral Surgery* 10 (1):6–13. doi:10.1007/s12663-011-0183-3.

Mohammed, M., A. Fitzpatrick, S. Malyala, and I. Gibson. 2016. Customised design and development of patient specific 3d printed whole mandible implant. In *Proceedings of the 27th Annual International Solid Freeform Fabrication Symposium*, 1708–17.

Paulo, R. 2005. Default priors for Gaussian processes. *The Annals of Statistics* 33 (2):556–82. doi:10.1214/009053604000001264.

Pechenin, V. A., M. A. Bolotov, and N. V. Rusanov. 2014. Method of evaluation of profile form and shaped surfaces with application of wavelets. *Research Journal of Applied Sciences* 9 (11):820–4.

Poniatowska, M. 2009. Research on spatial interrelations of geometric deviations determined in coordinate

measurements of free-form surfaces. *Metrology and Measurement Systems* 16 (3):501–10.
Rengier, F., A. Mehndiratta, H. Von Tengg-Kobligk, C. M. Zechmann, R. Unterhinninghofen, H.-U. Kauczor, and F. L. Giesel. 2010. 3D printing based on imaging data: Review of medical applications. *International Journal of Computer Assisted Radiology and Surgery* 5 (4):335–41. doi:10.1007/s11548-010-0476-x.
Sabbaghi, A., T. Dasgupta, Q. Huang, and J. Zhang. 2014. Inference for deformation and interference in 3d printing. *The Annals of Applied Statistics* 8 (3):1395–415. doi:10.1214/14-AOAS762.
Tepper, M., and G. Sapiro. 2012. L1 splines for robust, simple, and fast smoothing of grid data. *arXiv preprint arXiv:1208.2292*.
Tibshirani, R. J., and J. Taylor. 2011. The solution path of the generalized lasso. *The Annals of Statistics* 39 (3):1335–71. doi:10.1214/11-AOS878.
Trench, W. F. 2001. Properties of some generalizations of kac-murdock-szego matrices. *Contemporary Mathematics* 281:233–46.
Turner, B. N., and S. A. Gold. 2015. A review of melt extrusion additive manufacturing processes: Ii. materials, dimensional accuracy, and surface roughness. *Rapid Prototyping Journal* 21 (3):250–61. doi:10.1108/RPJ-02-2013-0017.
van Baar, G. J., T. Forouzanfar, N. P. Liberton, H. A. Winters, and F. K. Leusink. 2018. Accuracy of computer-assisted surgery in mandibular reconstruction: A systematic review. *Oral Oncology* 84:52–60. doi:10.1016/j.oraloncology.2018.07.004.
Walker, E., and S. P. Wright. 2002. Comparing curves using additive models. *Journal of Quality Technology* 34 (1):118–29. doi:10.1080/00224065.2002.11980134.
Xia, H., Y. Ding, and J. Wang. 2008. Gaussian process method for form error assessment using coordinate measurements. *Iie Transactions* 40 (10):931–46. doi:10.1080/07408170801971502.
Xiao, J., N. Anwer, A. Durupt, J. L. Duigou, and B. Eynard. 2018. Correction to: Information exchange standards for design, tolerancing and additive manufacturing: A research review. *International Journal on Interactive Design and Manufacturing (IJIDEM)* 12 (2):767–8. doi:10.1007/s12008-017-0439-3.
Yang, K., and P. Qiu. 2018. Spatiotemporal incidence rate data analysis by nonparametric regression. *Statistics in Medicine* 37 (13):2094–107. doi:10.1002/sim.7622.
Yang, K., and P. Qiu. 2019. Nonparametric estimation of the spatio-temporal covariance structure. *Statistics in Medicine* 38 (23):4555–65. doi:10.1002/sim.8315.
Zang, Y., and P. Qiu. 2018a. Phase i monitoring of spatial surface data from 3D printing. *Technometrics* 60 (2):169–80. doi:10.1080/00401706.2017.1321585.
Zang, Y., and P. Qiu. 2018b. Phase ii monitoring of free-form surfaces: An application to 3D printing. *Journal of Quality Technology* 50 (4):379–90. doi:10.1080/00224065.2018.1508274.
Zhang, Z. 1994. Iterative point matching for registration of free-form curves and surfaces. *International Journal of Computer Vision* 13 (2):119–52. doi:10.1007/BF01427149.

Appendix A

Fast Gaussian process parameter estimation

Since the scanned data points $y_p(\boldsymbol{x})$ are approximately located at a two-dimensional regular grid of size $n_1 \times n_2$, we develop a fast Gaussian process based parameter estimation approach as follows. According to the Gaussian process model in (1), the negative log-likelihood function with regard to the unknown parameters σ^2 and $\boldsymbol{\theta} = (\theta_1, \theta_2)$ can be expressed by

$$\ell(\sigma^2, \boldsymbol{\theta}) \propto N \log \sigma^2 + \log |R| + \frac{\Delta \boldsymbol{y}^\top R^{-1} \Delta \boldsymbol{y}}{\sigma^2}, \tag{16}$$

where $N = n_1 \times n_2$ is the total number of data points collected from the scanned surface. By minimizing $\ell(\sigma^2, \boldsymbol{\theta})$ with respect to σ^2, we obtain that

$$\sigma^2(\boldsymbol{\theta}) = \frac{\Delta \boldsymbol{y}^\top R^{-1} \Delta \boldsymbol{y}}{N},$$

which can be substituted into (16). The object function of the maximum likelihood estimation becomes

$$g(\boldsymbol{\theta}) = \log |R| + N \log (\Delta \boldsymbol{y}^\top R^{-1} \Delta \boldsymbol{y}). \tag{17}$$

Since the N data points are collected on an $n_1 \times n_2$ regular grid, the correlation function in (3) lead to

$$R = R_1 \otimes R_2,$$

where R_1 is an $n_1 \times n_1$ matrix with the i, k-th element $\exp(-\theta_1 |x_{1,i} - x_{1,k}|)$, and R_2 is an $n_2 \times n_2$ matrix with the j, l-th element $\exp(-\theta_2 |x_{2,j} - x_{2,l}|)$. Denote $\rho_1 = \exp(-\theta_1)$ and $\rho_2 = \exp(-\theta_2)$. According to the properties of kronecker product and KMS matrix (Trench 2001), the objective function in (17) can be reduced to

$$\begin{aligned} g(\rho_1, \rho_2) = &- \frac{\log(1-\rho_1^2)}{n_2} - \frac{\log(1-\rho_2^2)}{n_1} \\ &+ \log \operatorname{tr}(\boldsymbol{T}_1 \Delta \boldsymbol{Y} \boldsymbol{T}_2 \Delta \boldsymbol{Y}^\top), \end{aligned} \tag{18}$$

where $\Delta \boldsymbol{Y}$ is an $n_1 \times n_2$ matrix with the i, j-th element $\Delta \boldsymbol{y}_{ij}$. $\boldsymbol{T}_i = (1-\rho_i^2) R_i^{-1}$ for $i = 1, 2$ is a tridiagonal matrix

$$\boldsymbol{T}_i = \begin{bmatrix} 1 & -\rho_i & 0 & \cdots & 0 \\ -\rho_i & 1+\rho_i^2 & -\rho_i & \cdots & 0 \\ & & \cdots & & \\ 0 & \cdots & -\rho_i & 1+\rho_i^2 & -\rho_i \\ 0 & \cdots & 0 & -\rho_i & 1 \end{bmatrix}.$$

Notice that

$$\boldsymbol{T}_i = T_i^{(0)} - \rho \left(T_i^{(1)} + (T_i^{(1)})^\top \right) + \rho_i^2 T_i^{(2)},$$

where $T_i^{(0)}, T_i^{(1)}$, and $T_i^{(2)}$ are $n_i \times n_i$ matrixes with $T_i^{(0)}$ been an identity matrix, $T_i^{(1)}$ and $T_i^{(2)}$ been

$$\begin{bmatrix} 0 & 0 \\ I_{n_i-1} & 0 \end{bmatrix} \quad \text{and} \quad \begin{bmatrix} 0 & 0 & 0 \\ 0 & I_{n_i-2} & 0 \\ 0 & 0 & 0 \end{bmatrix},$$

respectively. Therefore, $\operatorname{tr}(\boldsymbol{T}_1 \Delta \boldsymbol{Y} \boldsymbol{T}_2 \Delta \boldsymbol{Y}^\top)$ in (18) can be expressed by

$$\operatorname{tr}(\boldsymbol{T}_1 \Delta \boldsymbol{Y} \boldsymbol{T}_2 \Delta \boldsymbol{Y}^\top) = \boldsymbol{\rho}_1^\top M \boldsymbol{\rho}_2, \tag{19}$$

where, for $i = 1, 2$, $\boldsymbol{\rho}_i = (1, -\rho_i, \rho_i^2)^\top$, and M is a 3×3 matrix with elements

$$M_{11} = \mathrm{tr}(\Delta \boldsymbol{Y} \Delta \boldsymbol{Y}^\top), \quad M_{12} = \mathrm{tr}\Big(\Big(T_i^{(1)} + (T_i^{(1)})^\top\Big)\Delta \boldsymbol{Y} \Delta \boldsymbol{Y}^\top\Big),$$
$$M_{13} = \mathrm{tr}\Big(T_i^{(2)} \Delta \boldsymbol{Y} \Delta \boldsymbol{Y}^\top\Big),$$
$$M_{21} = \mathrm{tr}(\Delta \boldsymbol{Y}\Big(T_i^{(1)} + (T_i^{(1)})^\top\Big)\Delta \boldsymbol{Y}^\top),$$
$$M_{22} = \mathrm{tr}\Big(\Big(T_i^{(1)} + (T_i^{(1)})^\top\Big)\Delta \boldsymbol{Y}\Big(T_i^{(1)} + (T_i^{(1)})^\top\Big)\Delta \boldsymbol{Y}^\top\Big),$$
$$M_{23} = \mathrm{tr}\Big(T_i^{(2)}\Big(T_i^{(1)} + (T_i^{(1)})^\top\Big)\Delta \boldsymbol{Y} \Delta \boldsymbol{Y}^\top\Big),$$
$$M_{31} = \mathrm{tr}(\Delta \boldsymbol{Y} T_i^{(2)} \Delta \boldsymbol{Y}^\top)$$
$$M_{32} = \mathrm{tr}\Big(\Big(T_i^{(1)} + (T_i^{(1)})^\top\Big)\Delta \boldsymbol{Y} T_i^{(2)} \Delta \boldsymbol{Y}^\top\Big),$$
$$M_{33} = \mathrm{tr}\Big(T_i^{(2)} \Delta \boldsymbol{Y} T_i^{(2)} \Delta \boldsymbol{Y}^\top\Big).$$

By using the reduction in (19), the objective function for maximum likelihood estimates, and its corresponding gradient functions can be expressed by

$$g(\rho_1, \rho_2) = -\frac{\log(1-\rho_1^2)}{n_1} - \frac{\log(1-\rho_2^2)}{n_2} + \log \boldsymbol{\rho}_1^\top M \boldsymbol{\rho}_2,$$

whose derivatives can be easily obtained. The matrix M does not depend on ρ_1 and ρ_2. After computing the matrix M, the computational costs of function evaluations of the objective function and gradient functions will be extremely simple. Therefore, the calculation of the maximum likelihood estimates can be reduced greatly.